POLITECNICO DI TORINO

CORSO DI LAUREA MAGISTRALE IN INGEGNERIA MECCANICA

Dipartimento di Ingegneria Meccanica e Aerospaziale

Simulation on a Hydrogen Internal Combustion Engine

Analysing the Power-Unit of an Optical Accessible Engine

Relatore:

Prof. Alessandro Ferrari

Correlatori:

Prof. Malte Jaensch, PhD, MBA

Felina Armbruster, M.Sc.

Candidato:

Luca Coletta

Matricola:

299781

Anno Accademico 2022/2023

Simulation on a Hydrogen Internal Combustion Engine

Analysing the Power-Unit of an Optical Accessible Engine

Wissenschaftliche Arbeit zur Erlangung des Grades
Master of Science (M.Sc.)
an der Fakultät für Maschinenwesen der Technischen Universität München.

Betreut von   Prof. Malte Jaensch, PhD, MBA

Felina Armbruster, M. Sc.

Lehrstuhl für Nachhaltige Mobile Antriebssysteme (NMA)

Eingereicht von   Luca Coletta, B.Sc.

Via Prato 10

03044 Cervaro (FR)

Eingereicht am   München, den 04.10.2023

Erklärung

Ich versichere hiermit, dass ich die von mir eingereichte Abschlussarbeit selbstständig verfasst und keine anderen als die angegebenen Quellen und Hilfsmittel benutzt habe.

München, 04.10.2023

Acknowledgements

A conclusione di questa tesi, voglio ringraziare tutti coloro che mi sono stati vicini e mi hanno supportato incondizionatamente durante il mio percorso universitario.

Ai miei genitori e a mia sorella Sara, a voi che ci avete creduto tanto quanto me, a volte anche più di me: spero di avervi resi orgogliosi e di continuare a farlo nel futuro.

A zio Benedetto e ai miei fantastici nonni: Elena, Giuseppe, Pasquale e Lidia. Grazie per la vostra presenza costante, per i vostri infiniti insegnamenti, ma soprattutto per i fantastici "pacchi da giù", vera salvezza dello studente fuorisede!

Vi sarò per sempre grato, vi amo!

Table of Contents

List of Abbreviations

List of Figures

List of Tables

1. Introduction

In an ever-evolving energy landscape, directed more and more towards sustainability, the reduction of pollutant emissions and the development of alternative technologies for both land propulsion and energy generation for stationary applications, the following work is meant to be placed: in this sense, hydrogen has always been highly interesting from a technological point of view, especially when used in the context of ICE, taking advantage of the knowledge and know-how obtained in the development of classic gasoline engines [25].

However, the use of a fuel that has physical-chemical properties that differ from those of conventional fuels poses new problems and challenges. In particular, it has been observed that the hydrogen combustion process, under certain conditions, may be abnormal and therefore sub-optimal in order to achieve efficiencies comparable to, or even higher than those of traditional ICEs [7]. This aspect is of great interest especially in stationary applications: in these, in fact, the energy involved is high and therefore high efficiency as well as a significant reduction in pollutants emitted into the atmosphere are key imperatives for achieving green energy production.

The present thesis work takes the abnormal combustion phenomena mentioned above as its starting point. In order to investigate these phenomena in depth, modifications were made to the cylinder head of a large-bore H_2-ICE (Hydrogen-powered Internal Combustion Engine) for stationary applications, involving the insertion of two different kinds of optical access systems in the combustion chamber.
This modification, while allowing close observation of combustion, clearly leads to a weakening of the cylinder head structure itself. Furthermore, special attention must be paid to the optical equipment, which could be damaged by the temperature and stress fields. To prevent this from occurring, it is proposed to determine the stresses and temperatures reached at critical engine components (in particular the cylinder head) with modelling using the commercial simulation software ANSYS.
Starting with the individual components in contact with the engine head, their geometric simplification is carried out to allow faster processing in finite element software. Then the components are assembled using Catia V5 CAD modelling software and the resulting geometry is exported to ANSYS. At this point, materials are defined and the components are discretized defining a mesh; then, the boundary conditions of the problem are applied: this passage is obviously crucial for obtaining reliable results.

At first, in order to determine the thermal field acting on the component, a purely steady-state thermal simulation is performed; a static structural simulation follows to determine the stresses, and then the previous two simulations are combined to determine the combined effects of temperature and pure mechanical stresses. Downstream of this, a comparison is made between the original engine head and the one suitably modified to accommodate

the optical equipment, along with an additional simulation with higher in-chamber pressure caused by the aforementioned combustion anomalies. Finally, having identified the most critical areas, these are verified from both a static and fatigue point of view according to the FKM guideline, determining the respective safety coefficients and factors of utilization.

The main aim of this thesis work is therefore to create an appropriate model that is as representative as possible of the main boundary conditions acting on the engine head itself and, downstream of the simulations carried out, to identify the critical zones that could be subject to failure. At the end, a complete evaluation of the stresses is provided, so as to examine both the thermal and mechanical resistance of both the head and endoscopes.

2. Basic principles

This chapter lays the theoretical basis for the studies that will be carried out later. First, emphasis is placed on hydrogen as an innovative fuel, possible application areas, advantages and disadvantages; after giving some basics on internal combustion engines, attention is drawn to individual components of the engine, especially the engine head (as emphasis lays on it regarding the later simulations) and the state of the art for current technology, then moving on to abnormal combustion phenomena and the main endoscopy technologies for ICEs. At the end, an explanation of the working principle of finite element software is given.

2.1. Hydrogen for sustainability

The world's industrial landscape is under constant pressure from the ever-increasing need to reduce pollutant emissions; most industries use fossil fuels for energy production, in addition to terrestrial propulsion. In this regard, internal combustion engines using fossil fuels generate about 25% of the world's power and they are responsible for about 17% of the world's GHG (Greenhouse gas) emissions [25]. In order to cope with the mitigation of climate change, as highlighted in the recommendations of Paris (COP21) and Glasgow (COP26) Climate Agreements [25] and with a view to drastically reduce emissions of pollutants and GHG, hydrogen can be a concrete and realistic fuel of the future.
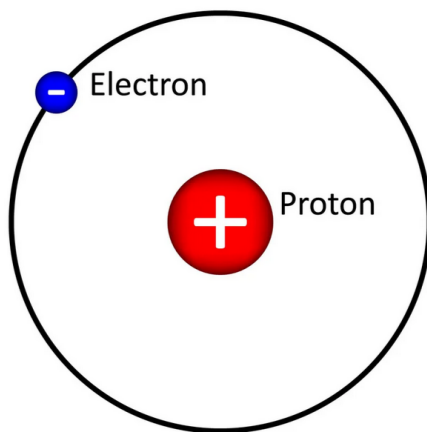
Figure 1 Hydrogen atom [30]
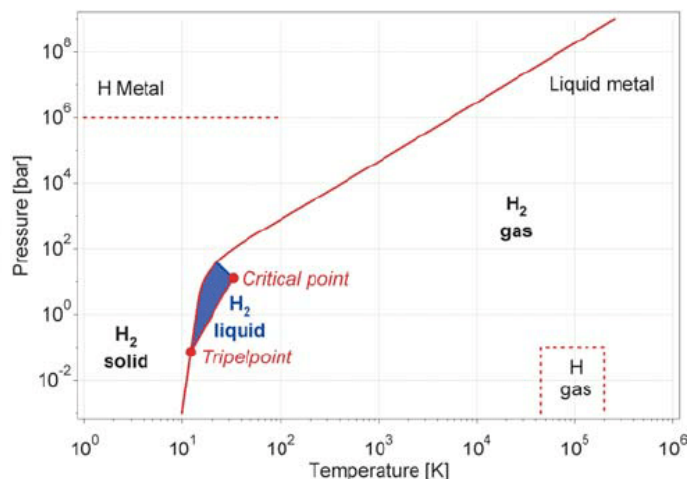
Figure 2 Hydrogen phase diagram [35]

2.1.1. Chemical-physical properties

Considering hydrogen from a purely chemical point of view, it is the simplest, smallest and lightest element existing on Earth. Taking a closer look to its atomic form, it has only one proton and one electron (Figure 1) and it is the latter, located in the valence band, that is responsible for its extreme reactivity [27]. As it can be observed in the phase diagram (figure 2), the range of existence for the gas phase is very wide, while liquid phase exists only for

very low temperatures (near absolute zero) [35]; this means that in order to achieve an energy density comparable to that of fossil fuels and to allow appropriate storage in relatively compact volumes, hydrogen requires a lot of mechanical work to compress the gas phase (maximum pressures up to 900 bars [16]) or alternatively it has to be cooled down to temperatures near to the absolute zero [35].

Table 1 shows the physical properties of hydrogen under standard conditions (T = 25 °C and p = 1 bar), comparing them with those of the most widely used fossil fuels. Among the most penalizing aspects, hydrogen has an extremely low liquid density (as much as 12 times lower than that of diesel) that, among other things, is reached under extreme temperature conditions. Also, minimum ignition energy is one order of magnitude lower than other fuels, along with a very high laminar flame speed: this is related to hydrogen extreme reactivity and poses new challenges concerning fuel injection control and combustion in ICE applications [8]. On the other hand, positive aspects include the high lower heating value, as well as the wide range of flammability and air to fuel ratio, parameters that ensure efficient combustion of the air-fuel mixture thus determining high efficiencies in different operating conditions.

Property	Petrol	Diesel	CH_4	H_2
Density (liquid) [kg/m^3]	750-770	820-845	432	70.8
Temperature [°C]	15	15	-62	-253
Lower calorific value [MJ/kg]	41.4	42.9	50	120
Energy density [MJ/dm^3]	31.7	35.8	21	8.5
Stoichiometric ratio [kg_{air}/kg_{fuel}]	14	14.7	17.2	34.3
Diffusion coefficient [cm^2/s]	0.05	-	0.16	0.61
Flammability limits [%vol]	1-7.6	0.6-5.5	4.4-15	4-76
λ range [-]	1.4-0.4	1.35-0.48	2-0.6	10-0.13
Minimum ignition energy [mJ]	0.24	0.24	0.29	0.017
Laminar flame speed [cm/s]	$\simeq 40$	$\simeq 40$	$\simeq 42$	$\simeq 230$

Table 1 Physical properties (under standard conditions): comparison among traditional fuels and H_2 [27]

2.1.2. Hydrogen production processes

One of the first challenges facing the realisation of hydrogen-based power generation is certainly hydrogen production. In fact, in addition to being the chemically simplest substance, it is also one of the most abundant on Earth, yet due to its reactivity it is rarely found in nature in its molecular form (H_2). Most hydrogen is in fact trapped in other molecules, including

water, fats, carbohydrates, proteins and hydrocarbons, and for this reason, it is necessary to produce it "artificially" using certain chemical compounds and appropriate amounts of energy [27].
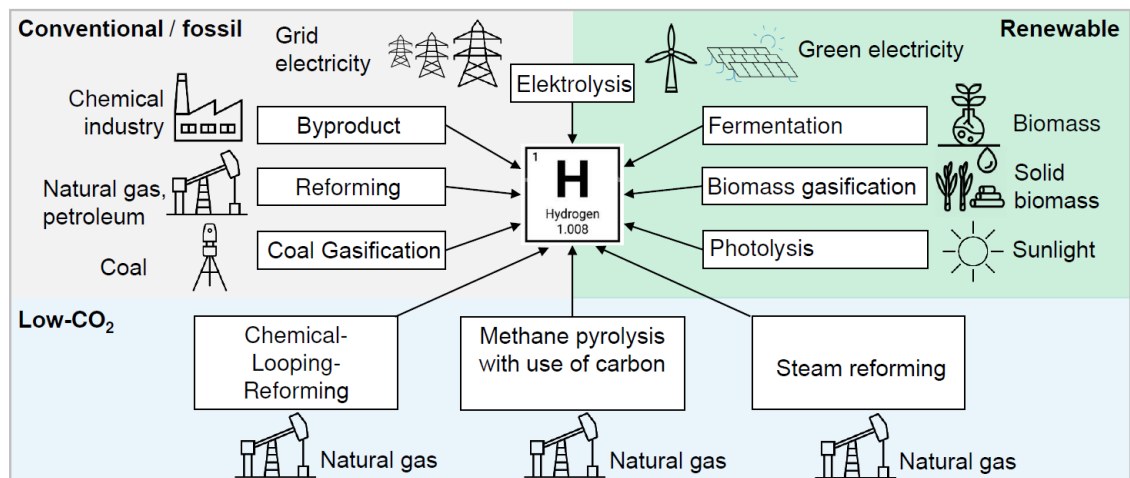
Figure 3 Overview of hydrogen production processes [27]

Figure 3 shows an overview of actual hydrogen production methods, with a breakdown in terms of the energy source used. In fact, they are classified in terms of environmental impact, starting from the conventional/fossil sources that have the greatest environmental impact, passing through low-CO_2 and finishing off with renewable sources: these latter are the most promising in terms of GHG emissions and, for this reason, they are constantly object of research.
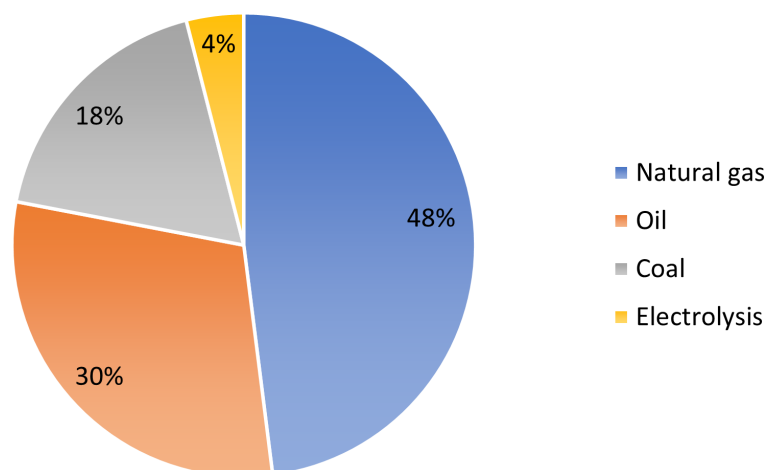
Figure 4 Hydrogen production (global) [27]

Going into much detail, figure 4 highlights the distribution of the most widely used substances

for global hydrogen production. Nowadays, in fact, nearly 50% of the hydrogen produced worldwide comes from the steam reforming process of methane; also, the natural gas used accounts for about 6% of global natural gas consumption [8]. Its diffusion is basically due to its high efficiency, near to 80%, and its cost of around 1,50 €/kg H_2, which is relatively low when compared with those of electrolytic plants [27, 25].

The SMR process takes place by subjecting the natural gas to temperatures between 700 and 900 °C and pressures between 20 and 40 bars, in the presence of a catalytic agent (typically nickel). The reaction that occurs under these conditions is as follows:

$$CH_4 + H_2O \rightleftharpoons 3H_2 + CO.$$

This is a strongly endothermic reaction ($\Delta H_{SR} = 206$ kJ/kmol) that requires a lot of energy to proceed. The industrial process then continues with the WGS (Water gas shift); this equilibrium reaction is as follows:

$$CO + H_2O \rightleftharpoons CO_2 + H_2.$$
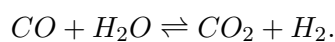
In this way, carbon monoxide is oxidized to CO_2 and additional hydrogen is produced. After the WGS, the different chemical species produced are separated through a PSA (Pressure Swing Adsorber) or membrane separator, obtaining hydrogen with a very high degree of purity [27]. A schematic of the entire SMR process is shown in figure 5.
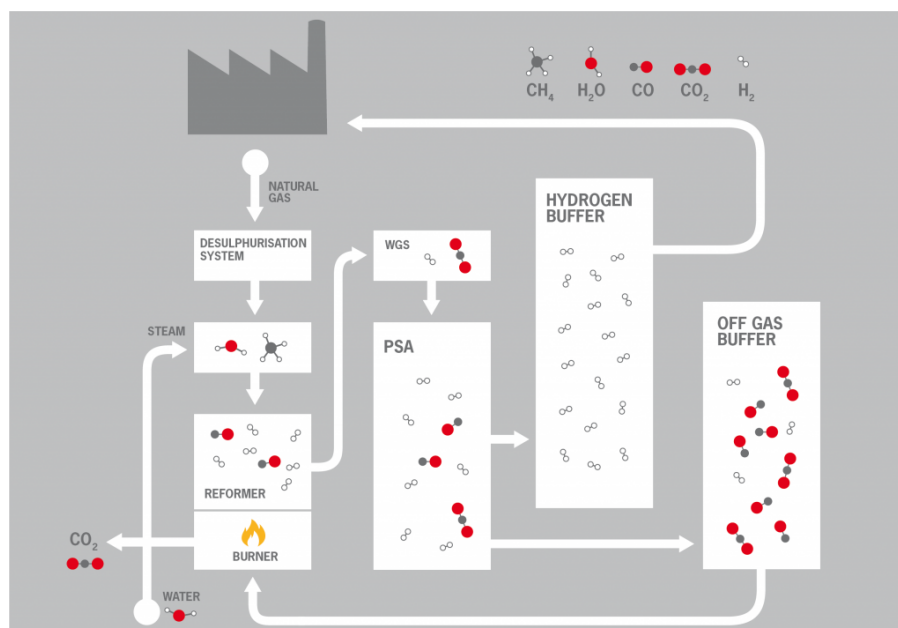
Figure 5 SMR process for H_2 production [11]

Along with steam reforming, a significant amount of the produced hydrogen is also due to partial oxidation reforming and autothermal reforming: partial oxidation reforming is a process mainly used for heavy hydrocarbons, such as by-products of petroleum refining but also oils and coal, which are exothermically reacted with oxygen at high temperatures and pressures (T = 1400 °C and p = 100 bars). This yields the so-called carbon monoxide-rich synthesis gas; then, exploiting the WGS reaction results in the oxidation of most of the CO to CO_2 and the production of H_2 with an efficiency up to 70% and a medium degree of purity, because of the soot production during combustion process [27, 25].

Autothermal reforming, on the other hand, is a hybrid technology between the two mentioned above: in this case, the heat of the exothermic reaction from the partial oxtidation reforming process is harnessed to make the endothermic reaction of steam reforming proceed. however, the need for high temperature to make the reaction proceed leads to the production of high amounts of nitrogen oxides, which are difficult to remove when the different gas phases are separated [27, 25, 34].

Another considerable fraction of globally produced hydrogen is due to the gasification process: this is essentially combustion in an oxygen-poor atmosphere and can be done either with coal or with waste and biomass; however, at present, biomass gasification for hydrogen production is still in a prototypical state, while the use of coal is definitely more widespread. Combustion produces a gaseous atmosphere that when subjected to high temperature allows the dissociation of hydrocarbons into various gaseous species, including hydrogen [27].
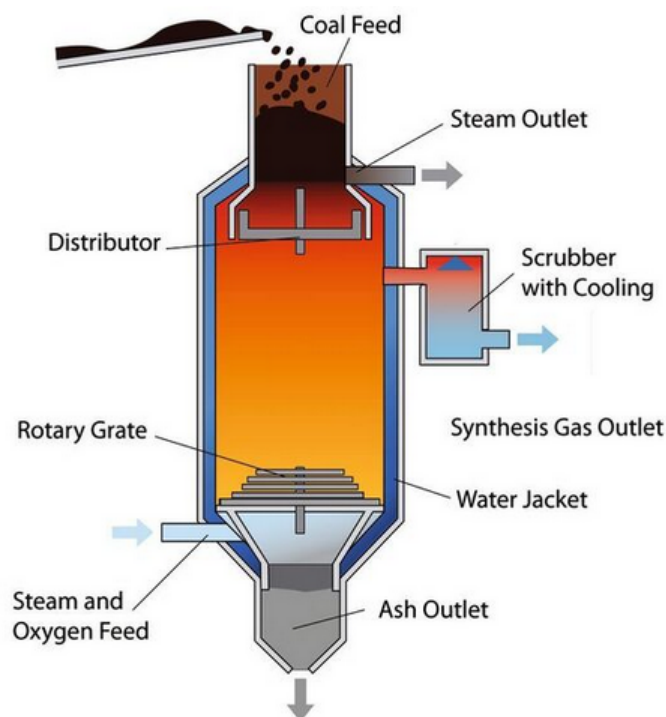
Figure 6 Coal gasification process [14]

This method, although relatively inexpensive, carries with it two major disadvantages: one is the high production of greenhouse gases, and the second is the low degree of purity of the hydrogen produced, due to the difficult elimination of particulate matter generated by coal combustion.

Instead, moving towards the production of so-called "green" hydrogen, electrolysis is the most promising technology [34]: this process is based on a series of redox reactions that basically leads to the division of the water molecule into its basic components in gaseous form, hydrogen and oxygen. Among the several industrial processes available, PEM has proven itself to be the most convenient.

$$4H^+ + 4e^- \rightarrow 2H_2$$

$$2H_2O \rightarrow O_2 + 4H^+ + 4e^-$$

$$2H_2O \rightarrow 2H_2 + O_2$$
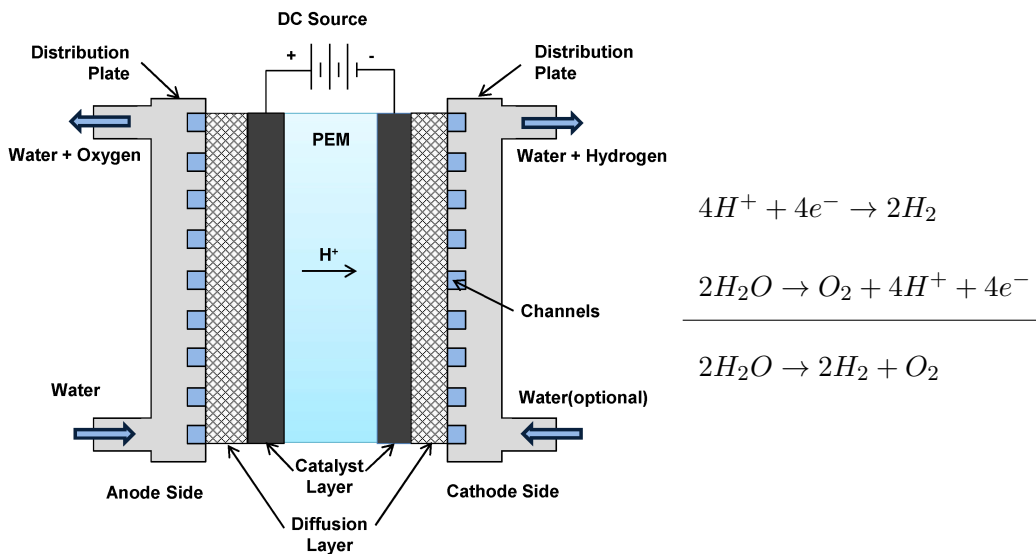
Figure 7 PEM electrolysis process [31]

The process takes place as described in figure 2.1.2: the water entering the anode is split, thus removing electrons and producing hydrogen ions; the electrons, thanks to the electromotive force given from an external DC source, move towards the cathode of the cell and reduce the previously formed hydrogen ions. A fundamental component of the cell is therefore the permeable membrane, which separates the cathode and anode but allows the flow hydrogen ions. The overall reaction is strongly endothermic (ΔH_R^0 = 286 kJ/kmol) and for this reason large quantities of electrical energy are required [34, 27]. This technology can certainly be encouraged by a wider diffusion of infrastructures to produce green energy from wind or photovoltaic power, thus exploiting hydrogen as an energy carrier given the transitory nature of these sources.

2.1.3. Storage and distribution

Due to its low density, hydrogen presents several technical and economic challenges to address. The most common storage methods are: compressed gaseous hydrogen, liquid hydrogen stored at temperatures of around 20 K, hydrogen in chemical compounds, currently under study [15].
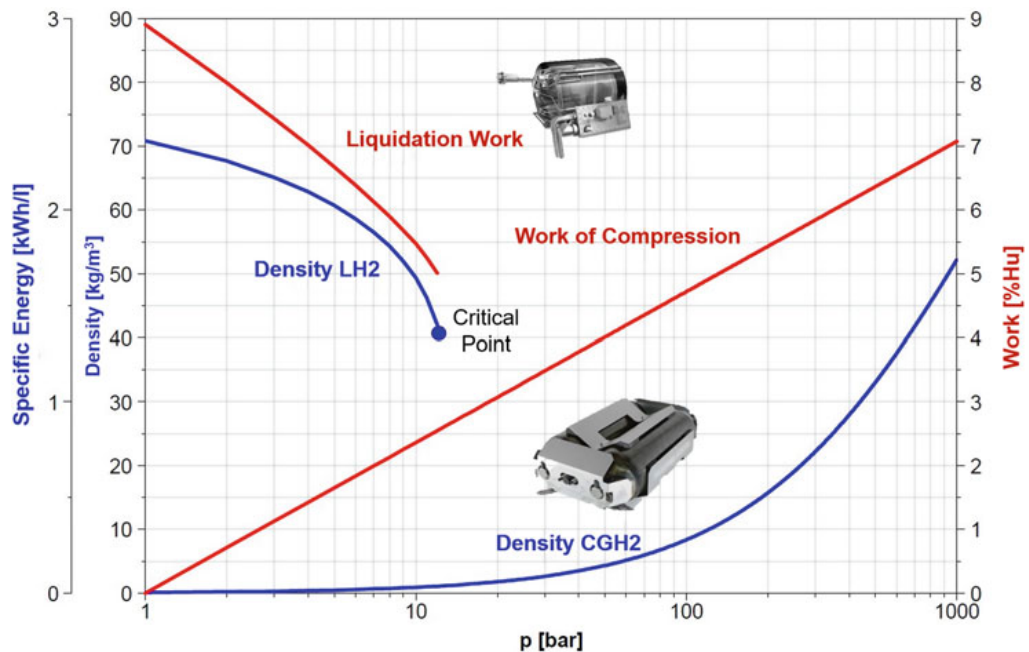
Figure 8 Storage density and work for hydrogen storage [15]

Figure 8 gives an overview of the volumetric energy density for different phases of hydrogen; it clearly shows that the highest energy densities are achievable with the liquid phase (up to 2,3 kWh/dm^3), while the gaseous phase at room temperature and limit pressures of 900 bar, has a density of only 1.6 kWh/dm^3. Moreover, the necessary compression work is also plotted in the diagram, as a fraction of the calorific value of hydrogen (120 MJ/kg). For the compression of the liquid an isobaric transformation has been assumed, while for the gas an isothermal transformation, both ideal. Considering the relative compression efficiencies, between 30% and 50%, it can be seen that a large amount of energy is needed for storage [15]. The situation also becomes even more complex when the volumetric density of the entire storage system is considered; in this regard, figure 9 compares the volumetric density of storage systems for different fuels. Two different aspects can be pointed out: at first, for the same volume occupied, the energy contained in a liquid H$_2$ storage system is only 1/6 that of a gasoline storage system. It is then equally interesting to note that while with liquid H$_2$ there is a loss of more than 50% between the density of the fuel alone and the entire storage system, in the case of gasoline or, for example, CNG (Compressed Natural Gas), this difference is much less noticeable. This can be justified by a greater complexity at the construction level of the whole system for H$_2$, which must obviously also include all the appropriate safety systems, which are necessary when dealing with a very reactive and flammable substance such as hydrogen [15].
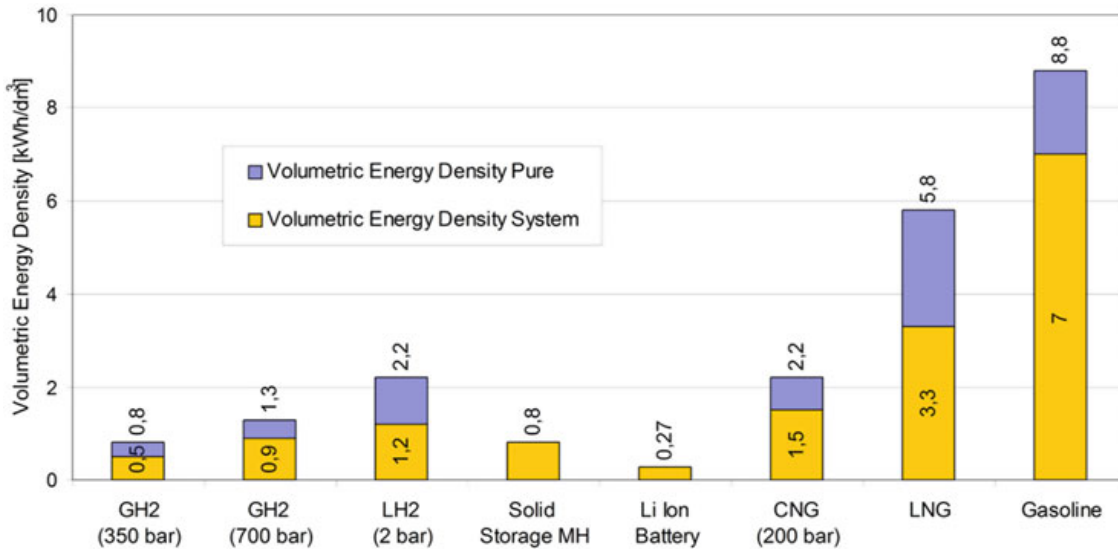
Figure 9 Volumetric energy densities of storage systems [15]

To close the summary picture on hydrogen, it is also interesting to make some considerations of an economic nature with a view to future developments. In this regard, picture 10 clearly highlights the reason why 96% of the hydrogen produced globally still comes from fossil fuels, and it's obviously a cost-related aspect [9].
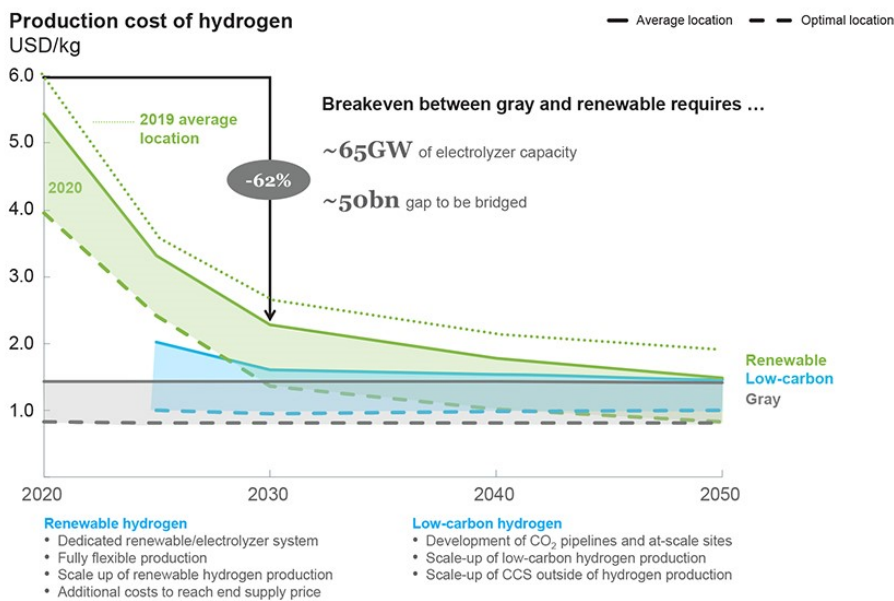
Figure 10 Hydrogen production cost [5]

However, a positive projection in favor of "green hydrogen" is shown, with a reduction in costs of 62% in the period between 2020 and 2030. Despite this, the gap compared to traditional and low-carbon technologies still seems too broad and difficult to fill in the short term. Nevertheless, the increase in the number of research projects involving hydrogen as a sustainable energy source, in the long term can lead to an increase in its visibility and consequently to further reduce its average cost on the market.

2.2. Internal combustion engines

For more than a century now, internal combustion engines have been the main source of mechanical power generation in the most wide-ranging fields of application. From marine to aviation, via the automotive and purely industrial sectors, with stationary applications, these fluid-driven machines have proved particularly versatile over the years, which is why they are still widely used today [3]. The following is a classification and explanation of the operating principles of these machines, as well as a description of the fundamental components, efficiencies and parameters important for their characterisation. In this regard, extensive use has been made of the contents from [3], [15] and [22].

2.2.1. Working principle and classification

A combustion engine is defined as a thermal machine in which the energy produced by the working fluid is transferred to one or more moving parts, which are capable of yielding a certain mechanical power to the user [3]. An initial classification can be made by distinguishing internal combustion engines, which have as their distinctive feature the repetition at regular intervals of the work cycle, from turbines, which do not have a real work cycle, being continuous flow machines. Both categories of machines, however, are thermal machines, meaning that chemical energy is converted into mechanical energy through the process of combustion of the air-fuel mixture. [3]

(a) Piston Engine

(b) Planetary piston engine (Wankel Engine)
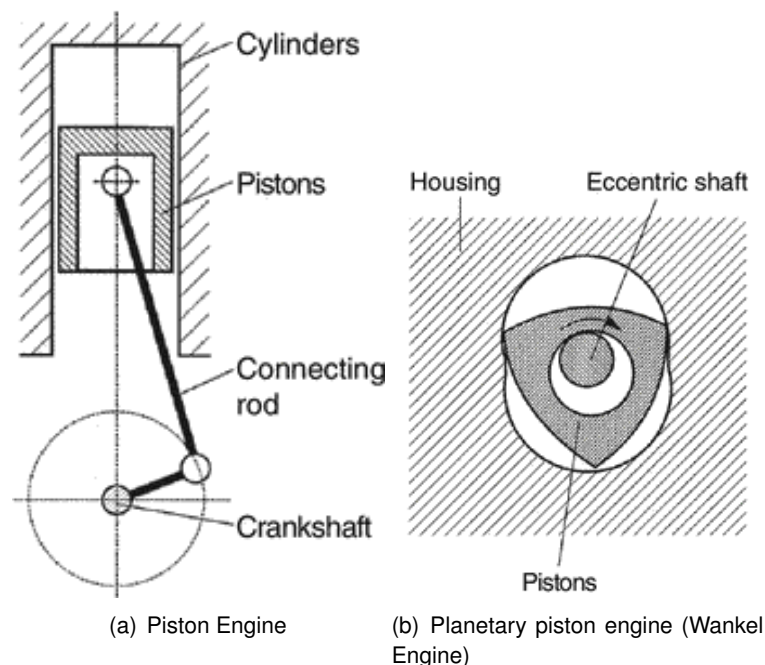
Figure 11 Working principles of ICE [3]

Figure 11 shows the most commonly used and studied types of internal combustion engine. In the vast majority of cases we are dealing with type (a), which has a cylindrical working

volume within which a piston, also cylindrical, moves. This is a classic connecting rod-crank system in which the crank is the driveshaft, which performs complete angular rotations; the connecting rod, on the other hand, describes an oscillatory motion, being bound on one side to the driveshaft, and on the other side to the piston, which is itself bound to move on a straight trajectory.

Wankel-type rotary engines (figure 11b), on the other hand, represent a very small slice of the global engine industry; several automobile manufacturers have become interested in this type of engine, due to its high power-to-weight ratio, small size and simple construction geometry. However, they have now fallen into disuse due to the disadvantages they bring with them, including the very high level of unburned hydrocarbons, high fuel consumption (especially when compared to engines of type (a)), low torque at low engine speeds and the difficulty in lubricating the segments at the apexes of the central rotor.

Further classifications may then consider:

- Combustion process;

- Fuel;

- Operating principle;

- Mixture formation;

- Configuration
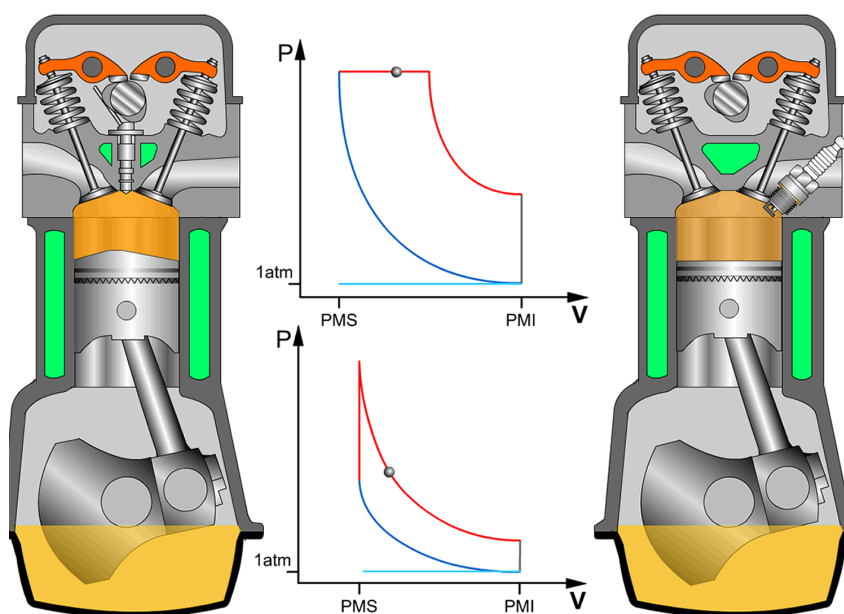
Figure 12 Otto vs Diesel cycle comparison [32]

As far as the combustion process is concerned, the most important distinction relates to SI (Spark ignited) and CI (Compression ignited) engines; in the former, after compressing the mixture of air and fuel, combustion is triggered by an external energy source (spark plug).

The reference duty cycle for this type of engine is the Otto cycle. In CI engines, on the other hand, combustion starts spontaneously: self-ignition of the mixture occurs due to the high temperature and pressure conditions in the combustion chamber; in this case, the reference cycle is the Diesel cycle.

This results in substantial construction differences, which are highlighted in figure 12: whereas in the engine CI only the injector is present in a central position (figure on the left), in the engine SI the presence of the spark plug is also required, which triggers combustion before TDC (Top Dead Center). One can also observe the difference between the two expansion processes on the diagrams shown, with isobaric expansion for the Diesel cycle and isochorous expansion for the Otto cycle.

Going into more detail, it is possible to introduce a classification according to the type of fuel, thus distinguishing liquid fuels such as the traditional diesel and petrol, as well as liquefied petroleum gases, paraffin and alcohols such as methanol or ethanol. On the other hand, gaseous fuels such as CNG, methane, propane, biogas and, of course, hydrogen are also very much in use. The latter is of particular importance in the context of this discussion because of its high potential to contribute to the reduction of pollutant emissions into the atmosphere.

A further distinction then concerns the operating principle of the engine itself, in terms of work cycle: it is possible to distinguish between 4-stroke and 2-stroke engines. Both types have in common the compression of the fresh charge of fuel-air with a reduction in the working volume and the ignition of the latter just before the motion of the piston is reversed, thus causing an increase in pressure in the cylinder which contributes to the production of mechanical work; the substantial difference lies in the way the exhaust gases are expelled and the new charge sucked in for the next cycle: while 4-stroke engines require an additional crankshaft rotation (half to eject the exhaust gases and half to re-inject new mixture with the intake process), in 2-strokes the ejection of the exhaust gases takes place in the vicinity of the BDC (Bottom Dead Center), thanks to the fresh charge at the intake. This mechanism is not particularly effective, in fact it is sometimes necessary to use a scavenging blower to improve the scavenging of the working volume. This inevitably entails a fictitious reduction in the volume available for the cycle, as well as a less effective exploitation of the air-fuel mixture due to the large quantities of unburnt fuel expelled into the atmosphere; for these reasons, 4-stroke engines are today the most widely used, thanks to their high efficiency especially when compared to 2-strokes [3, 22].

With regard to the gas exchange mechanisms, it is pointed out that in 2-stroke engines this is achieved by means of ports in the cylinder walls; in the case of 4-stroke engines, instead, it is carried out by means of a system of valves, which can have different actuation systems. The most widely used in modern applications is the OHV configuration, in which the valves are positioned in the upper part of the engine head: by means of a cam mechanism, the valves (intake and exhaust) are appropriately opened or closed to allow the exchange of the working fluid. The camshaft, which guides the opening and closing of the valves, can be positioned either in the crankcase or in the vicinity of the valves themselves, thus realising the OHC architecture: the construction differences are shown in the figure 13.
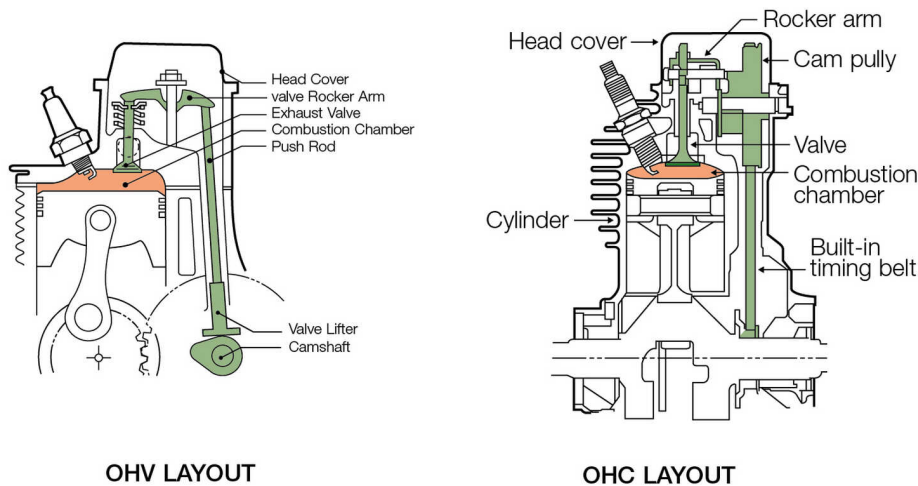
Figure 13 OHV vs. OHC configuration [24]

ICE can also be distinguished on the basis of the way the mixture is formed: one speaks in this case of a mixture formed internally, in the case of the DI (Direct injection) engines (such as the one to be simulated later on), or externally, as in the PFI (Port fuel injection) engines. The two technologies show differences in terms of charge homogeneity: more homogeneous in the case of PFI, less homogeneous in the case of DI; however, with the advent of electronic fuel management systems via ECU (Electronic control unit), the most promising technology, also in view of future developments, turns out to be the latter.

To conclude the classification of the ICE, the difference between supercharged engines and so-called naturally aspirated engines should be highlighted: whereas in the latter the air is sucked in exclusively thanks to the vacuum created in the cylinder, in the former the filling process is aided by a compressor, which generates a pressure greater than atmospheric pressure and allows the filling coefficient to be increased. The compressor can be coupled to the engine in direct drive on the crankshaft (mechanical supercharging) or by means of fluid-dynamic coupling, in which the compressor is driven into rotation by a turbine, which in turn is driven by the exhaust gases exiting the engine.

In this way it is possible to:

· appreciably increase the power and torque output for the same displacement;

· maintaining constant power and torque, but using a smaller, more compact engine.

This second aspect is particularly interesting because it lays the basis for a practice that is very much in use today, i.e. engine downsizing: this strategy was born with the intention of optimising fuel consumption and is realised by trying to make the ICE work at the point of operation with the highest efficiency, which is among other things very close to the point where loads are high (high BMEP (Brake Mean Effective Pressure)), while reducing the displacement and thus also the fuel demand.

2.3. Hydrogen internal combustion engines

2.3.1. History and developments

The idea of implementing a hydrogen internal combustion engine is relatively recent: in fact, it originated in the early 1930s, when some researchers were achieving very promising results in converting conventional ICEs to hydrogen operation and improving overall efficiency by adding small amounts of hydrogen to the fuel of conventional engines [15].

(a) First hydrogen prototype engine, 1939   (b) Hydrogen Wankel prototype engine
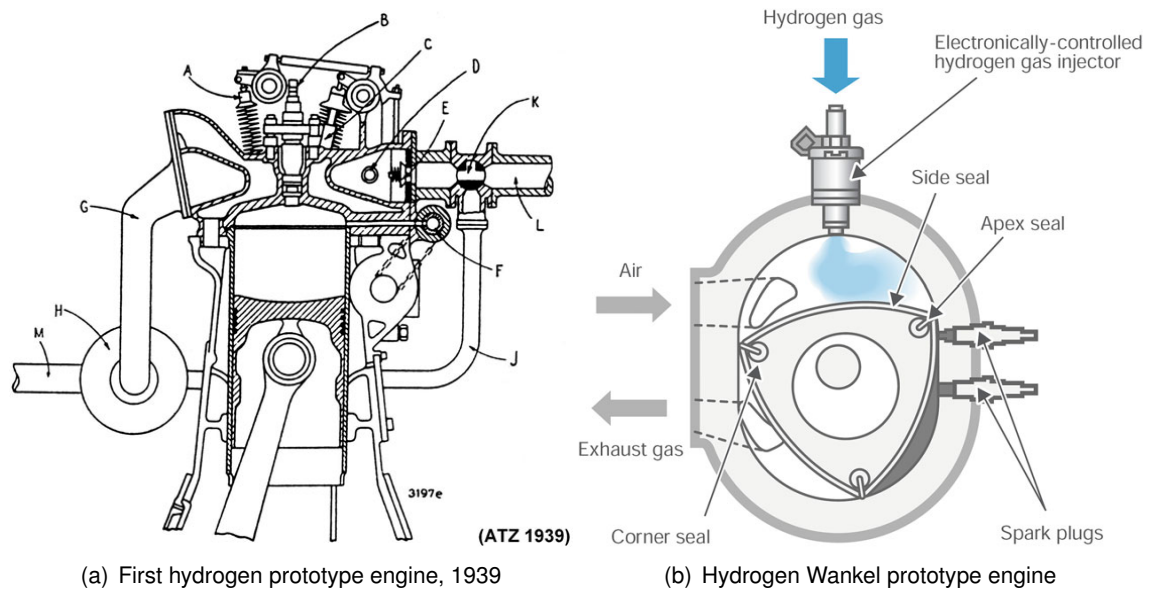
Figure 14 Hydrogen prototype engines [15, 12]

A first prototype is presented in figure 14a, while a much more modern one is depicted in figure 14a. For the Wankel rotary piston design and the related combustion chamber shape, the properties of hydrogen with its rapid flame propagation speed represent a favorable prerequisite [15] but unfortunately, because of the issues regarding the apex seals (see Section 2.1) this kind of engine is no more under development and almost the totality of research activity concentrates on reciprocating piston engines.

Nowadays, scientific research and experimentation in the field of H_2-ICEs follows several paths: first there is the will to achieve high efficiencies, and possibly comparable if not higher than those of conventional engines. Second, one has to maximize the potential of hydrogen as a green energy carrier, minimizing harmful emissions and greenhouse gases as much as possible. Much work is currently being done in the area of fuel injection strategies and mixture formation [15, 33].

Assumption:
$\lambda = 1$
λ_a = const.
η_e = const.
n = const.
V_D = const.

Fuel	Gasoline	Hydrogen	Hydrogen	Hydrogen
Mixture formation	Intake pipe	Intake pipe	Intake, cryogenic	Direct injection
Mixture temperature / K	293	293	210	293
Mixture cal. value / MJ/m³	3.59	2.97	4.14	4.21
Specific power / %	100	83	115	117

„State of the art" „Advanced/Research"

Figure 15 Full load potential for hydrogen mixture formation processes [15]

In particular, taking into account external mixture formation in connection with liquid storage, significant improvements can be achieved by injection of cryogenic hydrogen compared to the introduction of hydrogen at ambient temperature [15]. One advantage is based on the effect that the introduction of the cold hydrogen into the intake manifold leads to a cooling of the entire charge. The reduced temperature leads to an increase in the charge density and thus in the mixture calorific value [15]. Moreover, the fresh air charge has an extremely positive effect of the reduction of combustion anomalies, especially backfiring and pre-ignition [15, 25, 34]. Figure 15 shows the full load potential for different hydrogen mixture formation processes with respect to a conventional gasoline engine, putting in evidence that the cryogenic and direct injection mixture formation are technologies with the greatest development potential with regard to performance, efficiency and raw emissions. Regarding these last, the only harmful emissions to be kept under control are those from NO_x and to an almost negligible proportion those given by the combustion of small amounts of lubricating oil, since hydrogen has the great advantage of producing H_2O as a waste product of combustion. Regarding fuel injection strategies, there is a clear correlation between nitrogen oxides emissions injection time and air-fuel ratio: this is highlighted in picture 16. As the air-fuel ratio increases, there is a noticeable reduction in NO_x emissions, while looking at a curve with a constant λ ratio, it is observed that raw emissions decrease as ignition advance decreases. This fact can be justified by the stratification of charge in the combustion chamber: a richer mixture near the spark plug electrodes leads to very fast combustion, with high efficiencies, stable operation and reduced pollutants. Thus, in the case of engines for stationary applications, where loads are high and perforce the air-fuel ratio will be reduced, a useful strategy to mitigate emissions is to delay the start of injection until a few degrees before the top dead center [15]. This obviously has some drawbacks, leading to an increase of in-chamber pressure, which can reach values comparable to the ones of CI diesel engines.

Figure 16 Influence of injection time on NO_x emission behavior [15]

2.3.2. Importance of cylinder head

When it comes to hydrogen powered operation in ICEs, cylinder head is one of the most crucial engine components, determining a significant influence on: engine operation, produced power and torque, fuel consumption, emissions and acoustics [23, 3]. It performs a number of basic functions, including:

- sealing the combustion chamber at the top;

- housing the valve seats and valve guides;

- housing injectors and/or spark plugs;

- realizing adequate cooling of the parts most exposed to the flame front due to the mixture combustion;

- housing the passageways for lubrication of the moving parts.

This component is therefore exposed to loads of different kinds, such as: static loads due to the forced coupling of the valve seats and guides, as well as stresses due to the pretensioning of the screws that seal the head on the cylinder; crucial are also the dynamic loads due to the cyclically varying pressure in the combustion chamber and the ones due to the continuous temperature variation because of the high thermal gradients. Last but not least there is the corrosive effect given by the combustion gases, which in the case of hydrogen combustion is particularly relevant, since water has an extremely negative effect on ferrous materials.

2.3.3. Abnormal combustion phenomena

Many scientific studies, such as those conducted in [2], [7] and [13], have highlighted the influence abnormal combustion phenomena have in reducing ICEs engine efficiency, reliability and operating life. In the following an overview of the main abnormal combustion phenomena in the specific case of hydrogen is provided, along with the reasons why they occur and the possible strategies to mitigate them and their effects. Also, the main optical access systems are taken into account, as they are used a lot for research purposes in combustion.

One first major problem is represented by pre-ignition: it is a particular phenomena that consists of the early ignition of the air-fuel mixture; by definition, it occurs when both intake and exhaust valves are closed (i.e. during the compression stroke). On the basis of several studies conducted it has been pointed out that it takes place where there are simultaneously high temperatures and a locally too rich mixture [25];
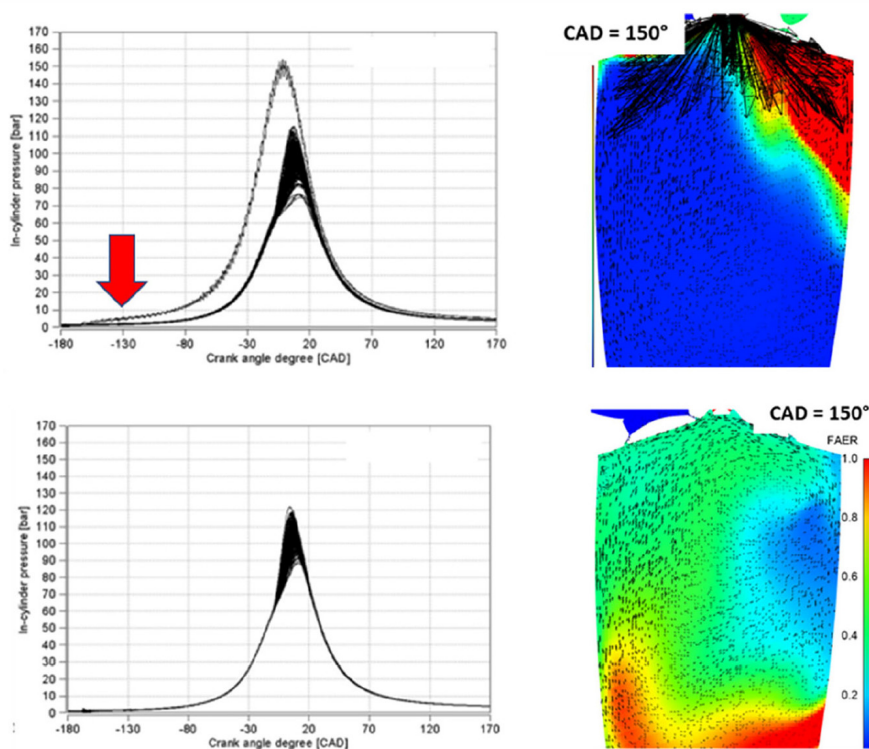
Figure 17 Impact of fuel distribution on the occurrence of pre-ignition [25]

More specifically, in figure 17 two different engine tests are performed with the same engine speed of 2000 rpm and fuel equivalence ratio of 0.5 (rich mixture). The first test (two figures on top) highlights the occurrence of pre-ignition at about 150 crank angle degree BTDC (Before top dead center), with a rapid increase of in-cylinder pressure if compared to normal operation. In order to investigate the root cause, CFD (Computational Fluid Dynamics) analyses such as those on the right of figure 17 have been conducted and they have shown that this behaviour is strongly influenced by charge distribution inside the combustion chamber: when the charge is stratified, pre-ignition is more likely to happen, especially around the exhaust valves and spark plug electrodes.

To overcome this issue, work can certainly be done on the aerodynamics of the combustion chamber, such as the increase of turbulence; moreover, one can focus on fuel injection strategies and timing; the aim is to obtain a high-quality, homogeneously-distributed air-fuel mixture that is certainly less prone to pre-ignition. [25] In addition, another adoptable strategy could be the reduction of the hot spots by using cold spark plugs, or even introducing a dedicated piston cooling and a specific lubricant [25].

Backfiring, on the other hand, is a slightly different phenomena. By definition, it is the abnormal pre-ignition of the fuel-air mixture during the gas exchange cycle and it can occur both in the combustion chamber and the intake manifold. It is related to the reduced hydrogen quenching distance and its extremely low ignition energy: when the mixture in the combustion chamber is locally rich, the flame can propagate even through very small gaps back to the intake manifold, causing significant damage to the intake system in relatively short periods of time. A research conducted at the Institute of Internal Combustion Engine at TUM on an H_2-ICE with a large bore optical access, have shown that one of the factors that most influences backfiring is the exhaust back pressure [7].
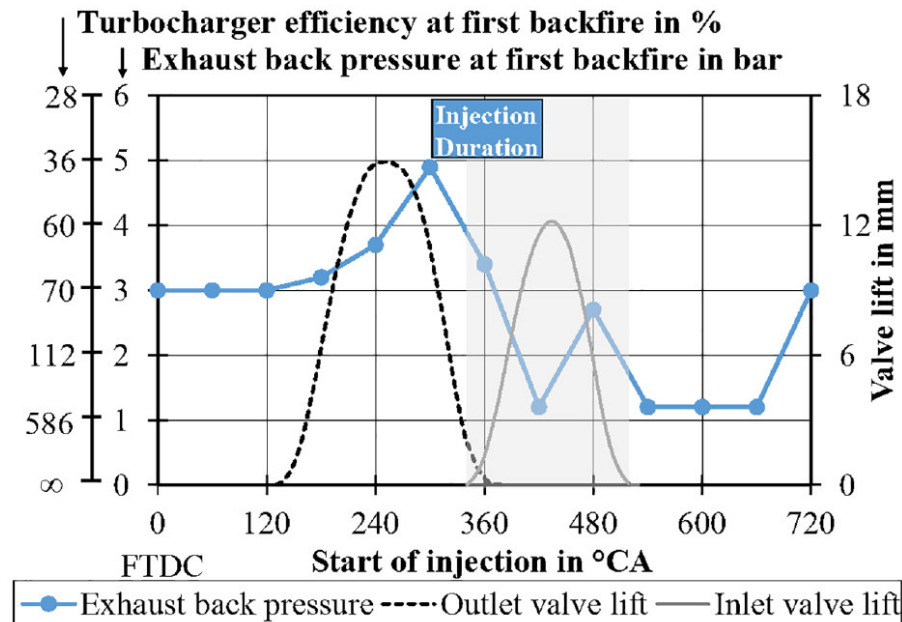
Figure 18 Influence of exhaust back pressure on the occurrence of backfiring [7]

In figure 18, start of injection is varied through 60° crank angle steps and for each value, the back pressure is incrementally increased until the first backfire occurs. The higher the back pressure reached, the less that point of start of injection is subject to backfiring. It shows that the best injection timing is the one at 300° crank angle; according to [7], it is probably because of the charge stratification in the intake manifold. Since the inlet valves open only after the injection, an air cushion is formed in front of the injected hydrogen cloud; by entering the combustion chamber first, this small amount of air lowers the combustion chamber surfaces temperature thus reducing the risk of backfiring.

On the contrary, injection in correspondence of 480° crank angle is very prone to backfiring. In this case, the injection takes place when the inlet valves are still closing; the flow velocity is

such that charge stratification is not achieved and thus contact between the charge and the exhaust gases causes backfiring by thermal ignition. This fact also leads to the hypothesis the phenomena is to be attributed to the hot gases around the exhaust valve, rather than to the hot surfaces [7].

A possible strategy that can be adopted to overcome this problem is the use of DI and a less rich air-fuel mixture, increasing the amount of air fed into the engine. In fact, compared to a classic state-of-the-art gasoline engine, an equivalent hydrogen engine can consume more than 50% more air, thus necessitating a suitable supercharging system (possibly two-stage) to send the right amount of air into the intake and achieve a power output comparable to a conventional ICE. Optimisation of valve timings and increased supercharging efficiency can also have a positive influence on the occurrence of backfiring, determining respectively a better charge stratification and a reduced exhaust gas temperature. Ultimately, it is also possible to consider reducing the compression ratio, but taking into account the inevitable deterioration in the combustion process.

2.3.4. Optical access investigations on ICEs

One of the most common practices to investigate more closely the combustion processes in a ICE is optical endoscopy: it is a measurement technique that is achieved by extracting images through optical equipment of various kinds [28]. For this purpose, it is necessary to have a camera (typically high speed) that extracts the images, positioned behind the display device; a lens system, inserted in a special metal housing, is then able to expand the field of view. As an example, a first type of endoscope is given in figure 19:

Figure 19 UV High Efficiency endoscope [17]

This apparatus is able to acquire images related to the spectrum of ultraviolet rays: this is useful when one wants to analyze the flame front propagation of the air-fuel mixture, as it is precisely defined by the light emissions given by the chemiluminescence of OH radicals in the combustion phase [19, 28]. Commonly, the most crucial component is the endoscope tip: it

has to perfectly seal the combustion chamber, and also has to withstand high pressures and temperatures coming from the combustion process. The component with the highest risk of failure, however, is the delicate lens apparatus, made of high-temperature-resistant glass, in this case up to 200 °C.
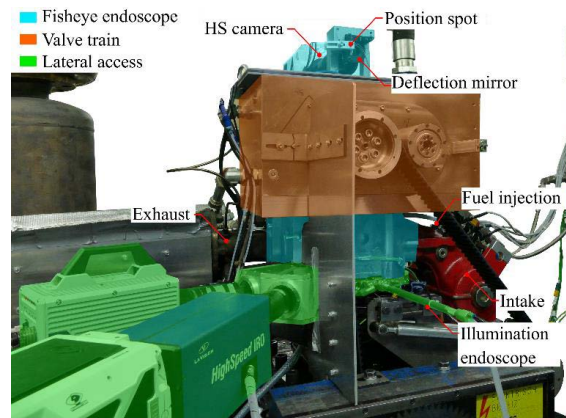
(a) Optical accessible engine setup
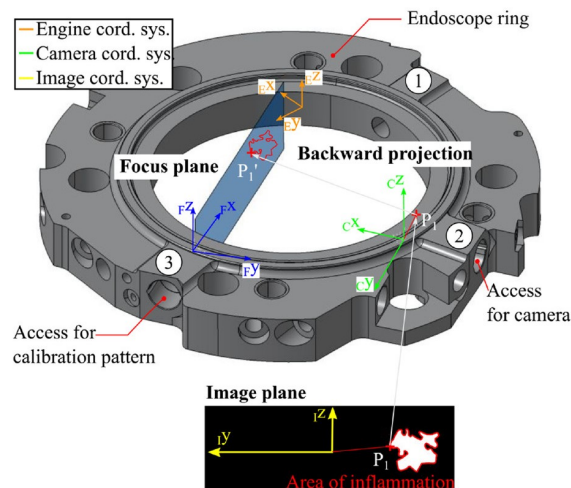
(b) Endoscope ring

Figure 20 Endoscope ring configuration [7]

These devices can be installed either directly on the engine head, as in the case study analyzed in this paper, or in a special endoscope ring (figure 20b), used for the optical endoscopy studies conducted in [7]. This last is a metal ring that is interposed between the cylinder head and the cylinder liner. It has a series of holes that hold the endoscopes, as well as numerous ducts that can cool them with compressed air.

In order to realize also a view from the top, another kind of endoscopic access can be implemented: with reference to the figure 20a, in the upper part of the cylinder head there is a fisheye-type endoscope [13]. It has a wider field of view and its installation is more invasive than the device in figure 19. In fact in the researches conducted in [13], in addition to those related to this paper, the fisheye endoscope required the removal of one of the two exhaust valves, thus reducing structural resistance and inducing potentially unwanted vibrations during engine operation.

Finally, a different kind of optical access is represented by transparent components [10], such as the cylinder liner. In this kind of application, the right choice of material plays a crucial role: quartz glass seems to be the most appropriate, combining an acceptable mechanical resistance and obviously the required transparency for the application. With such a technology, one has also the possibility to investigate the gas exchanges inside the engine, the influence of turbulent flows and even charge stratification, admixing a tracer substance to the injected fuel [10]. The images are captured with the Planar Laser Induced Fluorescence (PLIF) technology, while a possible experimental setup in depicted in figure 21.
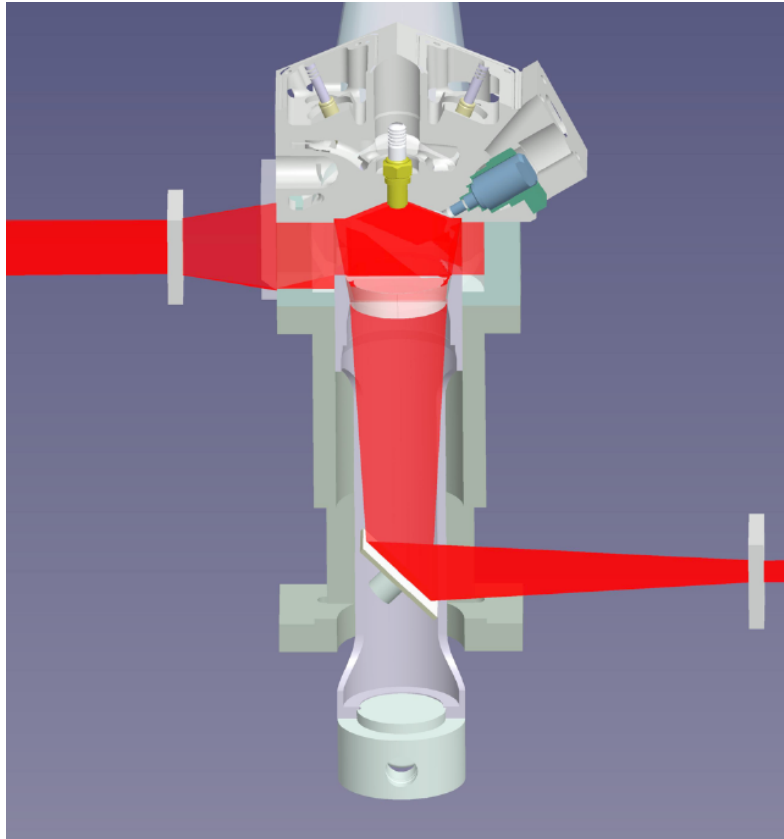
Figure 21 Transparent engine [10]

2.4. FEM simulation softwares

In modern industrial production, an increasing level of complex geometries, speed of production and adaptability of the latter to possible design changes during the prototyping phase is continuously demanded; at the same time, customers are more and more demanding and require ever shorter lead times for the realisation and development of products and processes. For these reasons, the use of FEM simulation software (such as Ansys) has become widespread.

The finite element method (FEM) is a general numerical approach for solving partial differential equations. To solve a general engineering problem using the FEM, the continuum system is firstly discretized into finite elements, which are connected by nodes, and then a collection of discrete elements is used to represent the original continuum system, as shown in figure 22 [20].
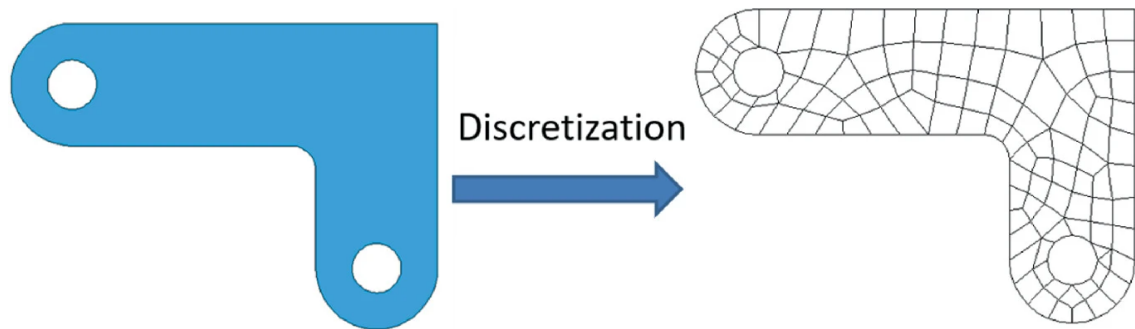
Figure 22 FEM discretization process [20]
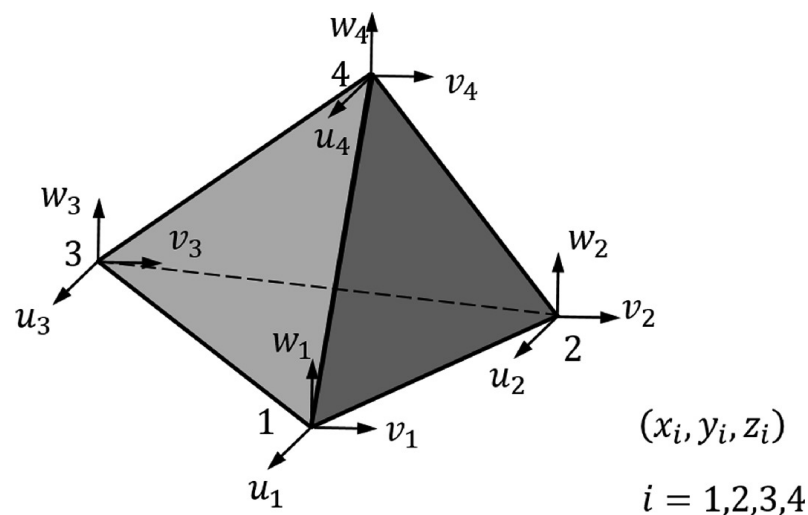
Figure 23 4-node tetrahedral element [20]

Discretization can be accomplished with different types of elements: one-dimensional, two-dimensional or even 3D. The use of the latter type defines what is known as finite-volume discretization, which is precisely what most of modern simulation software uses to solve problems of engineering interest in any domain, whether steady-state or time-dependent. How-

ever, it should be pointed out that unlike the real case, external stresses, be they stresses, strains or temperature fields, are not applied directly on the individual element of the discretization, but rather at its nodes. This assumption is necessary because of the nature of the mathematical model implemented [20]. It is worth to point out that the discretization process definitely plays a crucial role in a well-set up simulation: depending on the problem being studied, it is necessary to choose a shape (tetragonal, hexahedral) and a mesh element size that achieves the right compromise between the accuracy of the results obtained and the computational effort required by the computing device.

As an example, figure 23 depicts a generic tetrahedral element; each node, assuming the intention to perform a structural analysis, is characterised by a maximum of 6 degrees of freedom: three rotations and three translations, around the main axes x, y and z.

Under the assumption of elasticity there is direct proportionality between stresses and strains, as described by Hooke's law:

$$\sigma = E \cdot \varepsilon \qquad (2.1)$$

the constant of proportionality, in the most general case, is represented by the stiffness matrix **K**:

$$F = [\mathbf{K}] \cdot u \qquad (2.2)$$

F and u are the vectors containing the stresses and strains (both rotations and translations) at the individual nodes of the discretization, respectively. The aim of the simulation software is, in this case, to solve a different linear algebraic equation for each element of the discretization.
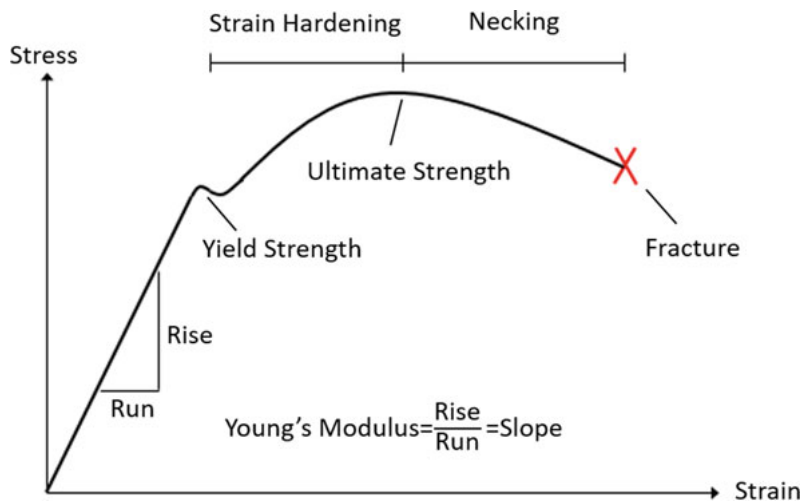
Figure 24 Steel stress-strain curve [20]

However, linear elastic behavior in some cases may not be adequate to describe the behavior of materials: just think of the stress-strain curve of a ductile material, such as steel (figure 24). In this case, the elastic assumption holds only up to the yield strength, after which nonlinearities take over [4].

This is where simulation softwares are mostly used, since the solution of complex partial

differential equations and big linear algebraic systems by hand calculation is quite difficult most of the times. Another interesting aspect to point out is that, because of the discretization of the domain, the same governing equations have to be discretized themselves.

By the way, the simplification of a complex physical problem through the use of the computer, thus virtualising the design and simulating the behaviour of a real component/assembly, makes the entire production process (from engineering phase to final production) much more flexible and ready to accept any changes, whether they concern geometry rather than the choice of materials or boundary conditions; this entails a significant reduction in costs due to the fact that it is no longer necessary to make real, functional prototypes for each change made; it is simply a matter of changing the model made on the computer and observing the effects of the changes on it. Although the aforementioned softwares are an enormous help for designers and engineers to keep up with the evolution of the industrial world, it should not be underestimated that the engineer's own sensitivity and common sense in choosing the right parameters and doing preliminary hand calculations always remain crucial aspects that cannot be neglected for the positive outcome of any project.

3. CAD model and simplification

This chapter will first provide an overview and carry out a description of the test bench developed at the Chair of Sustainable Mobile Drivetrains. It then proceeds to highlight the crucial components being simulated, proposing a simplification of these in order to optimize simulation time and quality and defining the final assembly, ready for the simulation process.

3.1. MTU Engine Test Bed

Figure 25 shows a three-dimensional rendering of the test bed developed at the Chair of Sustainable Mobile Drivetrains of the Technical University of Munich, developed with CATIA V5 CAD modelling software [18].
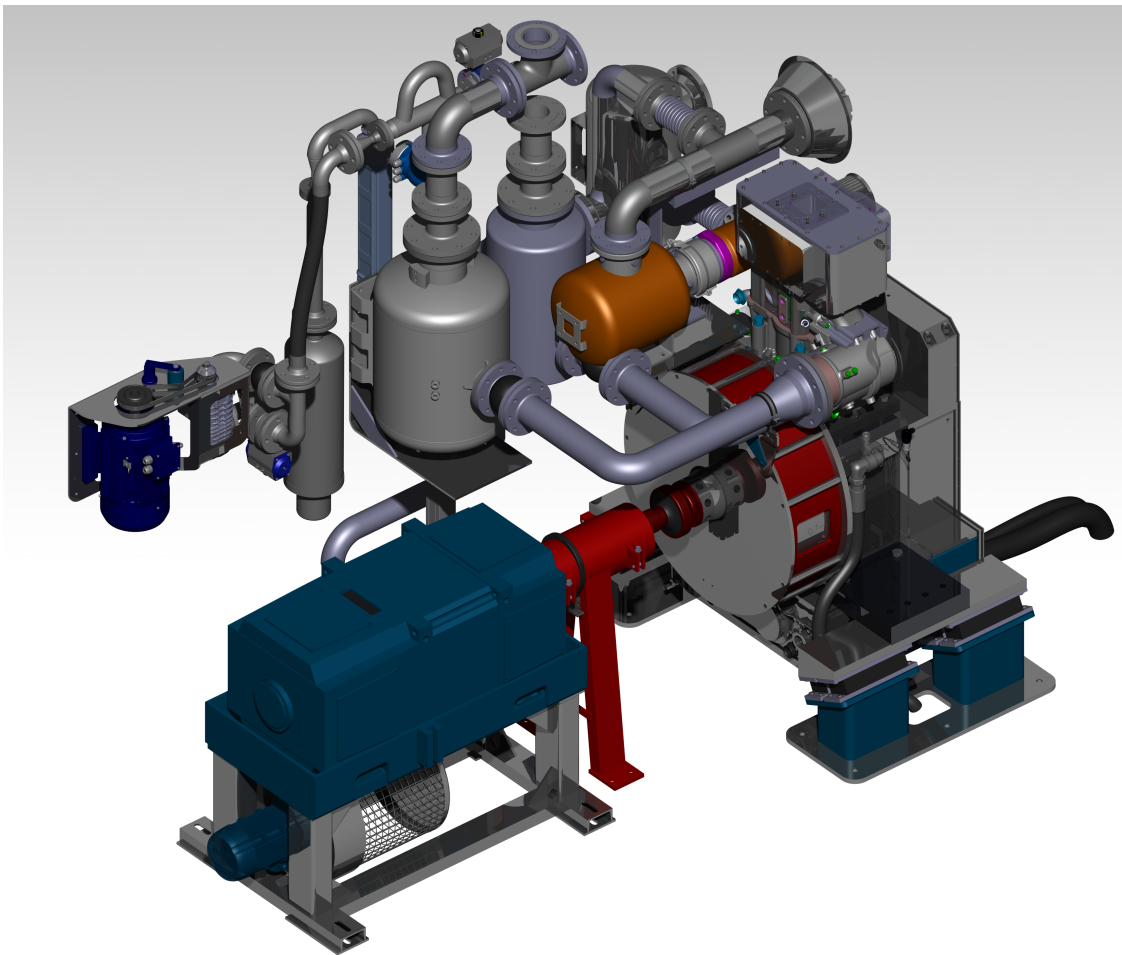
Figure 25 Complete engine model

The research engine consists of several components; wanting to make a subdivision into functional subgroups, we identify:

· **Propulsion system assembly**, consisting of valvetrain, cylinder head, cylinder liner, and

related engine crankcase;

· **Engine gearbox assembly** (located at the front in the figure representation 25);

· **Flywheel assembly** (in red, with its protective drum), which is responsible for smoothing the angular speed of the crankshaft;

· **Fuel assembly**, crucial for admitting the fresh charge into the engine via the IVs (Intake valves);

· **Exhaust gas recovery unit**, with the task of eliminating exhaust gases from the engine via the OVs (Outlet valves) and at the same time performing an analysis of them from the point of view of flow rate, presence of pollutants (such as NO_x) and possible unburned;

· **Electrical machine assembly**, with which the real behavior of the engine is simulated from the point of view of work load. Such an electric motor is connected by means of a special coupling to the crankshaft in such a way as to allow a complete characterization of the H_2-ICE as the rotational speed and the IMEP (Indicated Mean Effective Pressure) change.

3.1.1. Propulsion system

In this discussion, attention is focused on the heart of the entire system, namely the single cylinder propulsion unit shown in figure 26, whose technical specifications can be found in table 2.

Characteristic	Description
Architecture	Single Cylinder
Bore	170 mm
Stroke	210 mm
Displacement	4,77 l
Compression Ratio	from 10 to 15
Valves	2 inlet valves, 2 outlet valves
Engine speed	1500 rpm

Table 2 Test engine specifications, [2]

Fisheye endoscope

Spark plug

Endoscope lighting

Endoscopic
lateral access
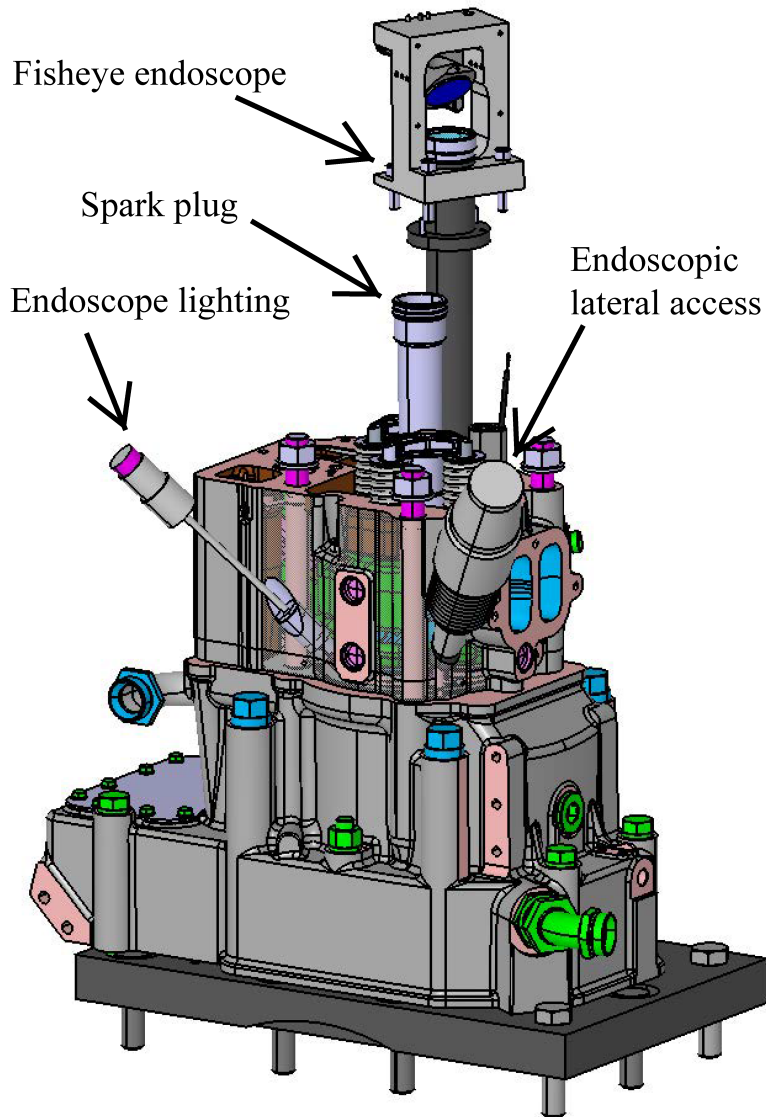
Figure 26 Complete engine with endoscopes

As noted, the engine head supplied by the manufacturer MTU has been suitably modified in order to accommodate additional components (supplied by the manufacturer LaVision), used specifically for combustion phenomena research purposes. Specifically, one has:

· An **endoscopic side access** via UV camera on the right side (see pdf in Appendix A for more details);

· An **illumination apparatus** (on the left) to allow the interior of the combustion chamber to be observed even in suboptimal lighting conditions;

· A **Fisheye-type endoscope** equipped with a high-speed camera and a system of mirrors that allow the positioning of the camera itself on a special stand, inclined with respect to the vertical direction. This last component, given its significant size, required the removal of one of the exhaust valves to enable its installation, in addition to the implementation

of an enlarged housing that has to be attached into the cylinder head itself, weakening it further.

The two bores for the side endsocopes are also designed in the same way, so that the positions of the lighting and recording apparatus are interchangeable. In order to include these additional components, it was necessary to increase the size relative to the height of the header itself; this modification, in order to avoid an increase in overall dimensions (already quite high for a system equipped with vertical Fisheye optical access) and to avoid having to redesign the entire distribution system, consequently required reducing the height of two plates: the first one seals the crankcase at the top (see figure 26) while the second, not shown in the figure, sits on top of the cylinder head. Being the base of the valve train assembly, it houses the camshafts and distribution lubrication ports. For these reasons, in addition to the engine head, it will also be necessary to verify these two components for structural simulation purposes.

3.1.2. Engineering data and material properties

As shown in figure 27, the definition of material properties in ANSYS is definitely straightforward: for the menu on the left one can choose all the different parameters for any kind of material; parameters are listed by category, highlighting basic mechanical properties such as those of linear elastic behaviour, but also those related to fatigue (S-N curve) and thermal coefficients.
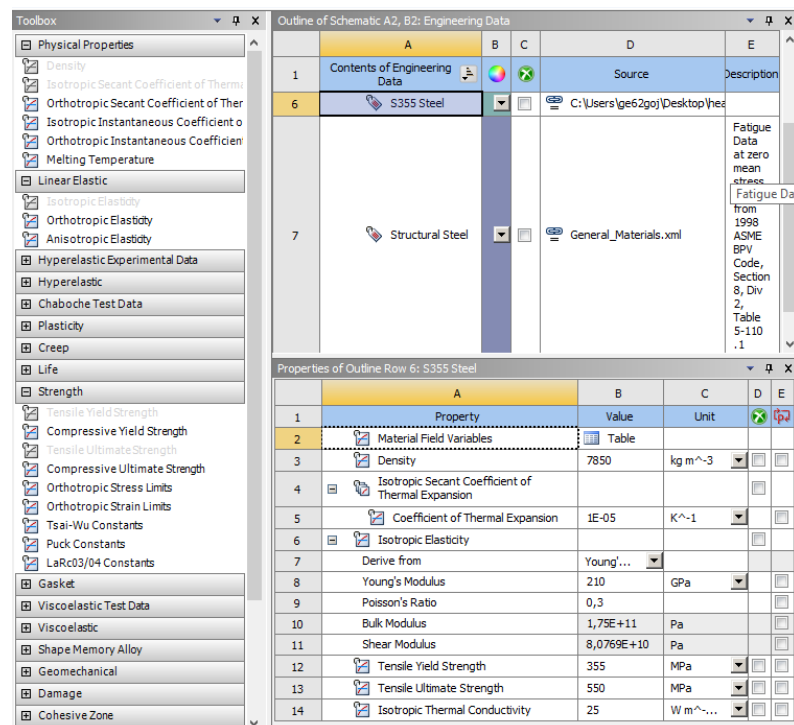
Figure 27 Engineering data interface

For the present work, several kinds of materials were used: grey cast iron for the engine head, S355 structural steel for the top crankcase cover plate and bottom valvetrain cover

plate, copper alloy for the sealing rings in the endoscope assembly and titanium alloy for the outer tube of the endoscope lighting system (see Geometry section for details). Table 3 lists the various physical properties for each material set inside the simulation software, while table 4 lists the material used for each component:

	GJL-250 Cast Iron	S355 Steel	Copper alloy	Titanium alloy	
Rp_{02}	-	355	280	930	MPa
R_m	250	550	430	1070	MPa
Young modulus	100,5	210	110	96	GPa
Compressive strength	840	550	430	1070	MPa
Density	7200	7850	8300	4620	kg/m^3
Thermal expansion coefficient	1,20E-05	1,00E-05	1,8E-05	9,4E-06	K^{-1}
Thermal conductivity	46,5	25	401	21,9	W/(m*K)

Table 3 Material properties

Component	Material
Cylinder head	GJL-250
Top crank case cover	S355 Steel
Bottom valve train cover	S355 Steel
Outer tube for endoscope	Titanium alloy
Endoscopes body	Structural steel
Sealing rings	Copper alloy
Head and plates screws	Structural steel
Endoscopes lenses	Ceramic glass

Table 4 Material-component association

3.2. Geometry simplification

As shown also in the representation of figure 25, the components to be extracted for the simulation are characterized by a high geometric complexity; this would lead to simulations with excessive computation time, but without adding useful information. it is therefore necessary to carry out an appropriate simplification of the geometric entities, using appropriate CAD software. In this regard, it was decided to use SpaceClaim software, which is integrated into the ANSYS working environment, because, compared with CATIA, it has ad hoc functions that allow intuitive simplification of the model, thus preparing it for export to the ANSYS Mechanical simulation environment.

3.2.1. Surface division

This function was necessary to determine the exact surface at the bottom of the cylinder head where the combustion pressure is applied. The task is simply completed as shown in figure 28, by creating a new sketch and drawing a circle of 170 mm diameter, corresponding to the engine bore.

Figure 28 Combustion surface creation

3.2.2. Face removal and surface de-featuring

Opposite to the previous function, the "delete faces" function aims to simplify the geometry of those components that present unnecessary features, such as chamfers, fillets and bad conditioned surfaces that can lead to singularities in the simulation process. As an example, figures 29a and 29b represent the result of the simplification. The valve train cover plate is only taken as an example, as this kind of operation is performed for both the plates and other components in the final assembly.

(a) Valve train plate original 3D model   (b) Simplified valve train plate 3D model
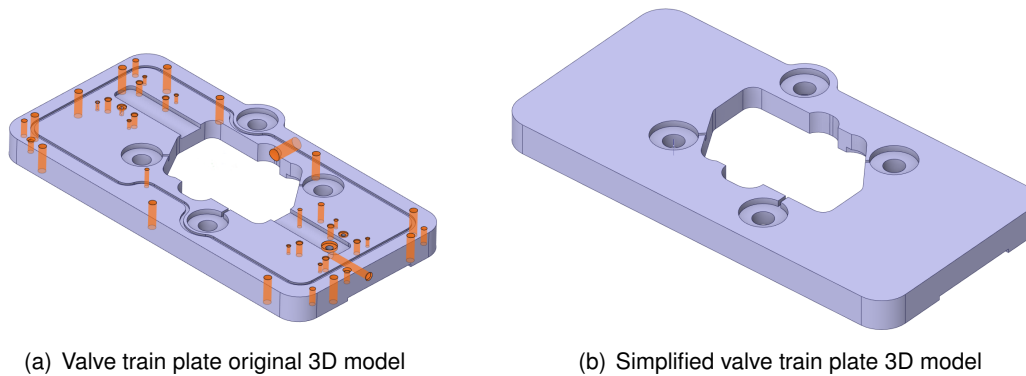
Figure 29 Valve train plate simplification

3.2.3. Cylinder liner

As the main focus of the simulation is the cylinder head with its optical equipment, it is necessary to correctly define the components adjacent to it; in the upper part is the valvetrain cover plate, while in the lower part should be inserted, strictly speaking, the original model of the cylinder liner. Again, in order not to make the model too heavy, an equivalent cylinder liner model was made (figure 30), consisting of a simple parallelepiped with the holes for the four cylinder head screws and the 170 mm bore hole. This allows, especially in structural simulations, a more realistic behavior of the assembly than the introduction of a simple fixed support at the bottom of the cylinder head.
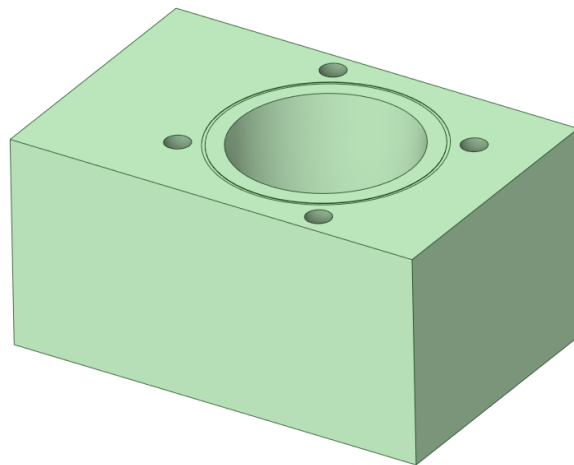
Figure 30 Dummy cylinder liner

3.2.4. Screws and nuts

A large number of hex head bolts and nuts are used in the original assembly, both to attach the crank case cover plate and to anchor the cylinder head to the cylinder liner. In this discussion, however, a simplification of these components is proposed, as the fittings, chamfers and hexagon faces of the bolts would only make the model heavier and slow down the calculation time, which is already quite high for a multibody simulation. Once again, use is made of

SpaceClaim to extrude an extremely simplified screw model with axisymmetric geometry ; it will be seen in the sequel how this aspect will be particularly advantageous to obtain as smooth a mesh as possible, improving the simulation result. By way of example, the figure 31 shows the four head screws with their nuts in their simplified form.
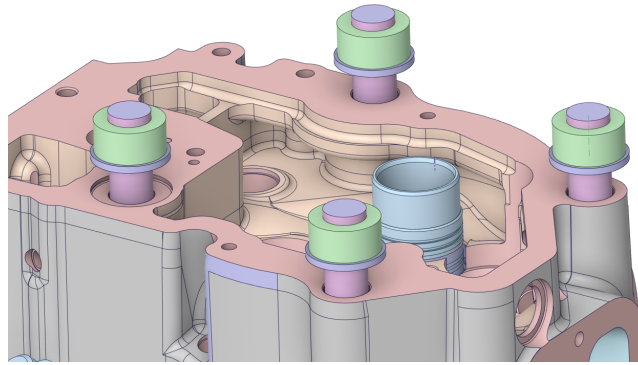
Figure 31 Simplified head screws and nuts

3.2.5. Endoscopes

The original models of the three endoscopes presents a lot of parts, such as lenses, focusing drives and the high speed cameras; however, since the crucial stresses are expected to take place in the proximity of the combustion chamber, only the essential components are kept in the model, with appropriate simplification especially for the endoscope lighting tube, necessary to hold the endoscope in place and also seal it to prevent cooling fluid leaking. Main modifications regard the removal of unnecessary fillets, and the correction of the bore-holes diameter in order to set a correct contact condition between the parts that are screwed together (see contacts section in the next chapter).
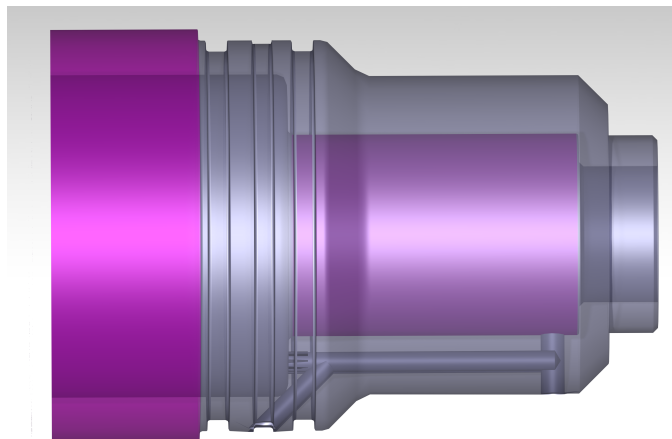
Figure 32 Endoscope sealing tube

3.2.6. Final assembly

With all the geometric simplifications made, the final assembly looks as in figure 33. This assembly will be used in the following to perform all the simulations and comparisons necessary to fully characterize the components of interest.
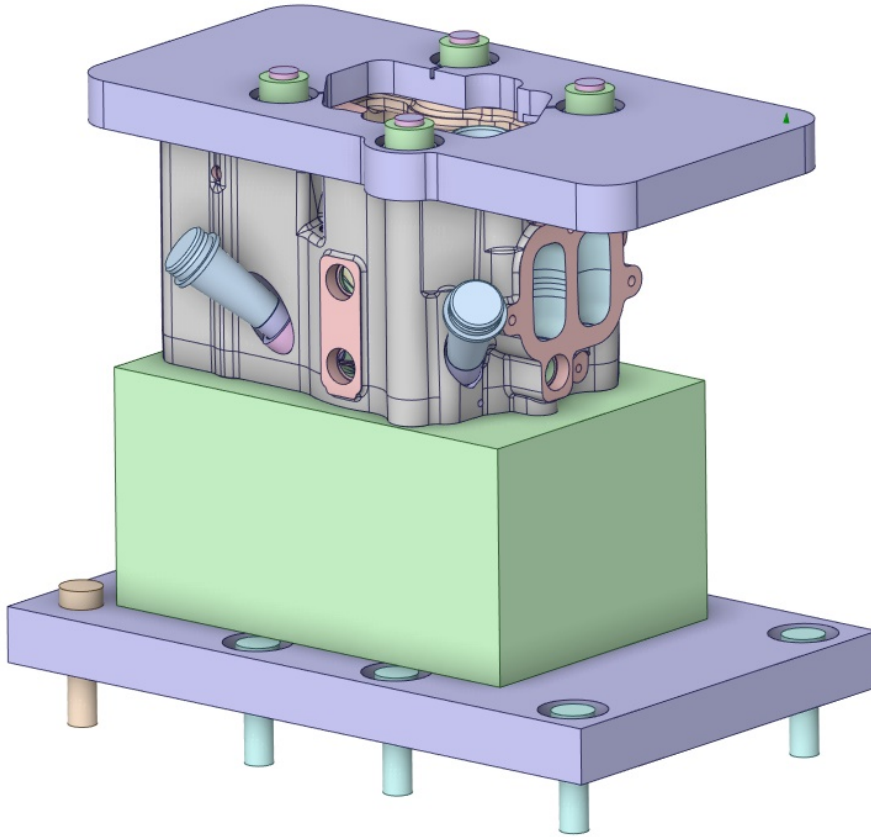
Figure 33 Complete simplified engine assembly

4. FEM simulations

The following chapter describes the methodology and approach used to perform both the thermal and structural problems, following a structured logical process from the selection of parameters and boundary conditions to the final solution.

4.1. Setting up a FEM simulation with ANSYS

Conducting a FEM simulation using the ANSYS software requires some basic steps [1], which will be explained below to familiarize the user with the working environment and the user interface. Upon opening the main interface of ANSYS Workbench, it is observed that different types of analysis can be selected from the menu on the left. Having identified the analysis one is interested in, for example "Static structural", we proceed to insert it into the workbench project by dragging and dropping the related item into the empty space on the right, as shown in figure 34a:

(a) Ansys Workbench user interface (b) Static structural block
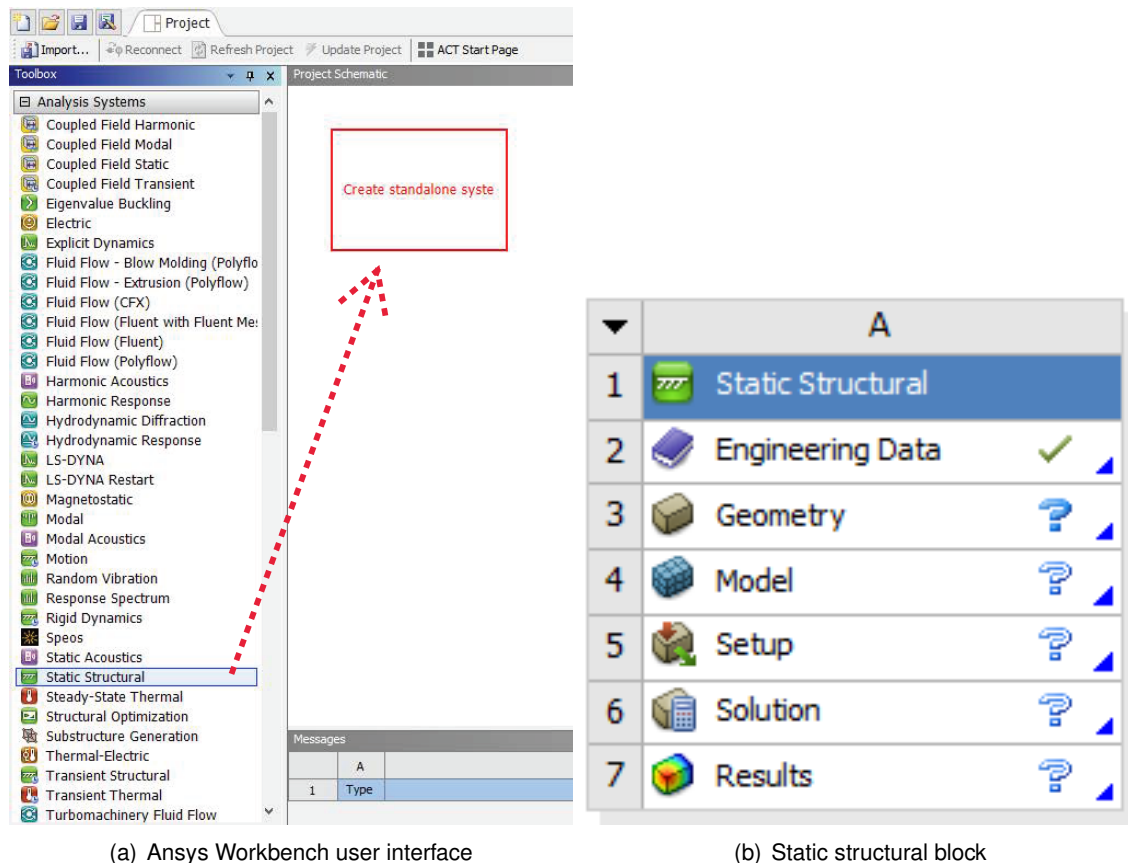
Figure 34 Ansys project initialization

The functional block depicted in figure 34b lists the series of sequential steps to be performed to achieve the desired results. For this reason subsequent subchapters, except the CAD (Computer Aided Design) geometry simplification already discussed in the previous chapter, will be structured in the same way.

4.2. Model setup

The setup of model parameters goes through the definition of certain characteristics that strongly influence the quality and reliability of simulation results [1, 20].

4.2.1. Meshing settings

Since the assembly depicted in figure 33 consists of many parts, some of which are very different sizes, ANSYS default settings for the size and shape of the discretization elements may not be appropriate. The software does, however, offer the option of changing various parameters at will, from defining more detailed mesh zones to choosing the shape of the elements and the faces or solids on which to apply these parameters.

Going into more detail, for the screws and bolts, simplified as shown in Chapter 3, an axisymmetric mapped mesh was chosen: this is to provide a fine and regular mesh, that leads to obtain accurate results with a high degree of reliability. The cylinder head is the component with the highest degree of geometric complexity and for that reason, it is also the most difficult to mesh; the discretization for this component is achieved by setting up a tetrahedral meshing, which is the default one for ANSYS. The average element size was chosen based on numerous tests conducted, in order to optimize the computational solving time of the model and still obtain acceptable results. Further modifications to the mesh in terms of local refinement were made in the contact zones between components, as well as in the zones where boundary conditions are applied (figure 35).

(a) Complete cylinder head meshing   (b) Mesh refinement for internal passages
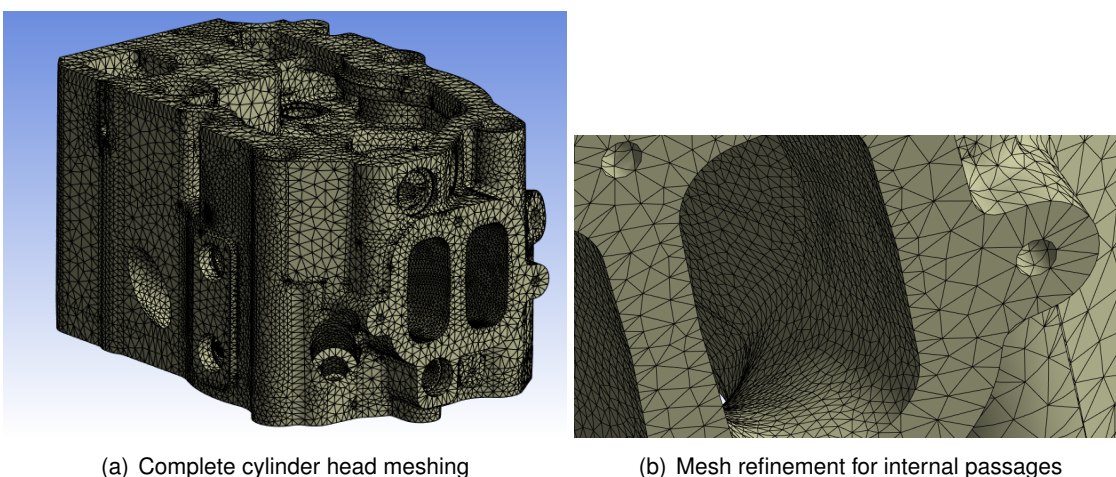
Figure 35 Cylinder head meshing

These modifications are especially crucial when one wants to simulate, as in this case, a convection phenomenon in which a fluid laps a solid and thus the transport of energy is

directly affected by the matter transport.

The table 5 summarizes all the mesh-related settings for both the thermal and structural problems.

Mesh settings		
	Thermal	Mechanical
Cylinder head element sizing	7 mm	
Head and top crankcase cover screws	Multizone method 5 mm element size, hexahedral	
Plates element sizing	7 mm	
Endoscopes element sizing	3 mm	
Combustion zone	1 mm refined face sizing	
Fisheye sizing	3 mm element size	
Whole assembly	-	Automatic method
Head internal passages for cooling fluid and inlet/outlet ports	3 mm mesh refinement	-
Contact interfaces for endoscopes screw connection	-	3 mm mesh refinement
Dummy cylinder liner	20 mm element sizing	

Table 5 Mesh settings for structural and thermal simulation

4.2.2. Contacts definition

Another crucial passage to correctly setup the simulation (especially the structural one) is the definition of contact zones between the different parts of the assembly; once again, ANSYS offers a variety of contact settings, shortly summarized in table 6:

Type	Separation	Sliding
Bonded	No	No
Rough	Yes	No
No Separation	No	Yes – frictionless
Frictional	Yes	Yes – frictional
Frictionless	Yes	Yes – frictionless

Table 6 Types of contact settings in ANSYS [1]

Depending on the components that come into contact with each other, one can choose the appropriate setting; the contact between the cylinder head and the liner, or between the liner and the crank case cover plate was modelled using a "bonded" contact definition: this is because these parts are not expected to be moving when subjected to loads during normal operation. A different discussion, however, relates to the screws, washers and bolts; these components are not supposed to be attached to the parts they are holding together without chances to move, but they are usually subject to little displacements after they have been preloaded. Being more specific, the contact interface between the washer and the cylinder head was modeled as rough: that means, realistically, that the washer cannot slide, but can move in the axial direction. The same reasoning has been applied to the interface between the nut and the washer itself. Bolted connections, such as those present in both plates, cylinder head and the endoscopes, represent another crucial contact situation: they are modelled as "frictional" contacts, simulating the friction between the bolt and the nut; however, a true modelling of the threads in CAD software and then their simulation in ANSYS would drastically increase computational time. It is then necessary to enable a specific setting, in order to allow the software understand that the connection between the parts is a threaded one and not simply a contact between cylinders. As shown in figure 7, contact geometry correction is enabled defining the "bolt thread" option and specifying the thread parameters.

Geometric modification	
Offset	0 mm
Contact geometry correction	Bolt thread
Orientation	Program controlled
Mean pitch diameter	24 mm
Pitch distance	2 mm
Thread angle	60°
Thread type	Single thread
Handedness	Right-Handed

Table 7 Contact geometry correction for bolt threads

4.3. Thermal boundary conditions

The boundary conditions for the thermal problem, especially for simulating realistic cylinder head behavior, are difficult to determine. For this reason, heat flow transfer in the cylinder head passages is a widely discussed theme in literature; among the different models currently available, one of the most widely used has proved to be the Woschni model [23]. Woschni's model has the peculiarity of estimating the velocity of the gas inside the combustion chamber; this velocity is given by the sum of two contributions: a mechanical contribution due to the movement of the piston, estimated by considering the velocity average of the latter as a representative quantity and a contribution due to combustion, since during this process there is an increase in fluid velocity that contributes to increase the convective heat transfer coefficient value.

In choosing these boundary conditions, therefore, a hybrid approach was followed, based, for the combustion chamber convective heat transfer coefficients, on previous thesis work such as [4] and [23], which dealt with similar heat transfer problems. The temperatures, instead, were the result of experimental measurements, performed with temperature probes directly installed in the engine under test and provided as input data for the simulation. In addition to defining convective heat transfer due to inlet and outlet gases, the presence of lubricating oil near valves and camshafts was also modeled. Since the oil exhibits a high heat capacity, it may be reasonable to assume a Dirichlet-type boundary condition, setting the temperature of the oil at 90 °C as found under operating conditions. The following figures depict the application zones of the aforementioned boundary conditions.

Description	Type of BC	Symbol	Value
Inlet port	Convection	h_{INLET}	1300 W/(m^2*K)
		T_{INLET}	318,15 K = 45 °C
Outlet port	Convection	h_{OUTLET}	500 W/(m^2*K)
		T_{OUTLET}	870,15 K = 597 °C
Combustion chamber	Convection	h_{COMB}	1200 W/(m^2*K)
		T_{COMB}	1070,15 K = 797 °C
Coolant flow (glycole)	Convection	h_{COOL}	2000 W/(m^2*K)
		T_{COOL}	363,15 K = 90 °C
Lubricating oil	Fixed temperature	T_{OIL}	363,15 K = 90 °C

Table 8 Boundary conditions for cylinder head thermal simulation

It is important to point out that these boundary conditions are conditions that are the result of time averaging over an entire work cycle; as an example, consider the fact that during

the combustion phase, the heat transfer coefficients in the combustion chamber are infinitely larger than during the intake phase. However, since the thermal analysis conducted is steady-state, it is consistent to assume parameters that are averaged over time, since transient behavior has not been modeled.
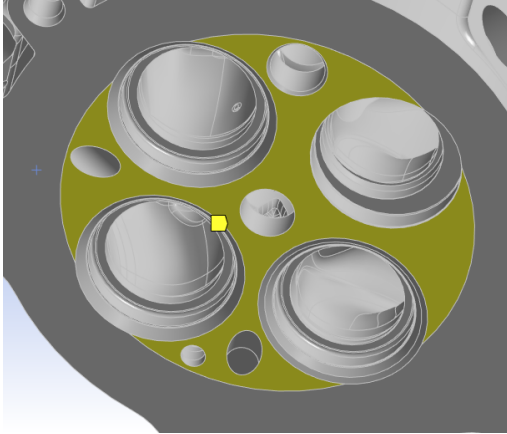
(a) Combustion chamber

(b) Inlet port
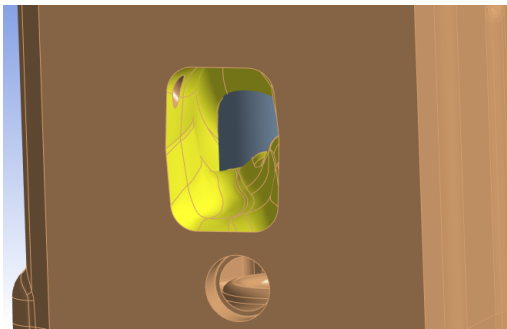
(c) Outlet port
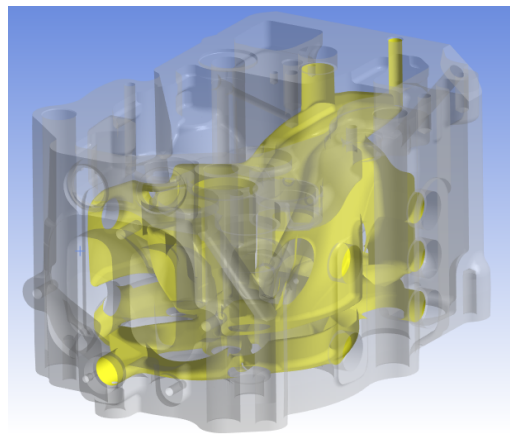
(d) Coolant flow
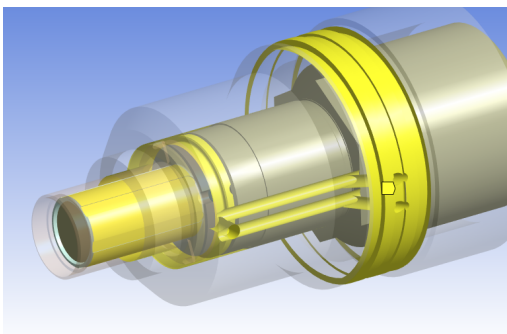
(e) Endoscope lighting cooling
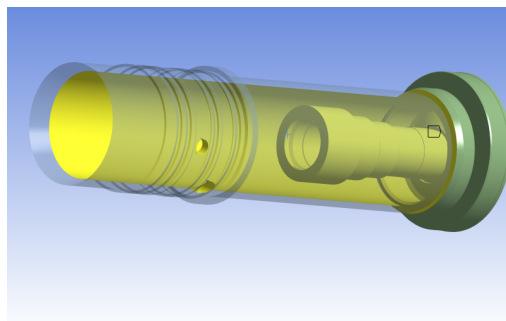
(f) Fisheye cooling

Figure 36 Thermal boundary conditions application zones

4.4. Mechanical boundary conditions

Mechanical boundary conditions mainly concern the forces due to tightening of screws and nuts, endoscopes, and the pressure generated as a result of combustion of the air-fuel mixture. At first, known the tightening torques, the axial pre-tensioning forces are computed using the following formula taken from [6]:

$$F_V = \frac{2 \cdot M_T}{d_m \cdot tan(\alpha_m + \phi') + d_t \cdot tan(\phi_s)} \tag{4.1}$$

where:

M_T; applied torque;
F_V: axial force given by torque;
d_m: thread mean diameter;
$tan(\phi') = \frac{tan(\phi)}{cos(\alpha)}$;
α: helix angle (30° for metric threads);
$tan(\phi)$: friction coefficient between screw and nut;
$tan(\phi_s)$: friction coefficient between underhead of the screw and washer;
$\alpha_m = \frac{p}{\pi \cdot d_m}$
p: thread pitch.

Then, an estimation of the mass of the valve train assembly, which lays on top of the plate, is performed using the "inertia" tool built in CATIA V5 [18], resulting in a total mass of about 260 kg.

Regarding peak in-chamber pressure, it has been experimentally determined on the test bench itself. However, two different values are chosen: a first one deals with normal operation of the engine, without combustion anomalies, while a much bigger value (400 bars) refers to the occurrence of combustion anomalies that, as already explained in Chapter 2, lead to an uncontrolled increase of combustion chamber pressure thus causing damages to the whole system in short periods of time. For this reason, the simulation has been carried out defining 3 different load steps:

1. **Non-fired operation**, only static loads from bolts pre-tensioning and endoscopes threaded connections;

2. **Fired normal operation**, with previous static loads plus a 250 bars in-chamber pressure;

3. **Fired overload operation**, simulating the occurrence of combustion anomalies and raising the combustion pressure to 400 bars.

Regarding the axial force for the threaded connection of the endoscopes, it is taken from a previous thesis work [29], while the endoscope lighting sealing tube had to be calculated (see Appendix A for details), resulting in an axial screwing force of about 16000 N on the M42 metric thread.

Table 9 summarizes all the mechanical boundary conditions applied to the model, while figure 37 shows part of their application on the 3D model.

Description	Type of BC	Value
Combustion peak pressure	Pressure	250 bar
Weight of valve train	Mass force	260 kg
Cylinder head screws pre-tensioning	Force	25000 N
Bottom end of crank case cover	Fixed support	-
Crankcase cover bolts pre-tensioning	Force	14000 N
Peak in-chamber pressure due to combustion anomalies	Pressure	400 bar
Endoscope lighting tube pre-tensioning	Force	16000 N
Endoscope lighting pre-tensioning	Force	5600 N
Endoscope pre-tensioning	Force	5600 N
Valve springs (each valve)	Force	1000 N

Table 9 Mechanical boundary conditions
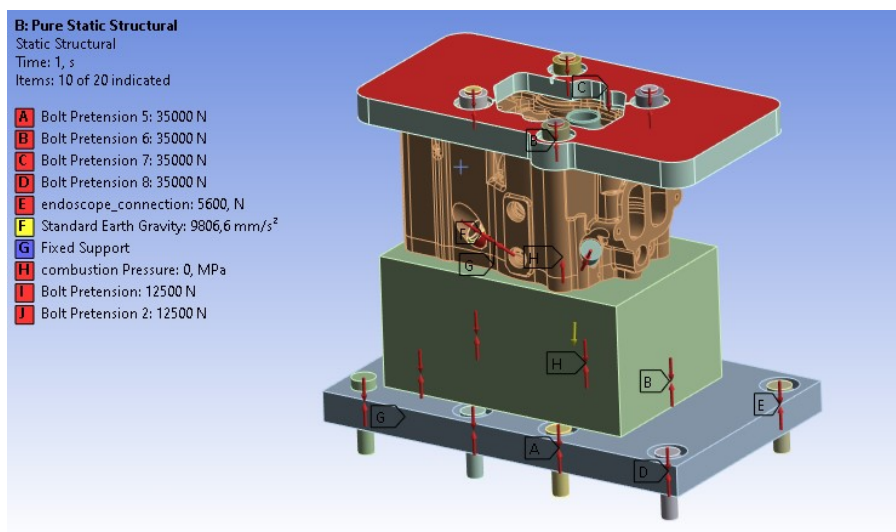
Figure 37 Mechanical boundary conditions

The exact connection of the fisheye to the cylinder head has not been simulated since it is still in the design phase; however, a frictionless contact condition between the two components has been implemented, so that at least an idea of the stresses that are created can be obtained.

5. Simulation results

5.1. Thermal simulation results

The following figures show the thermal field computed for the main components: cylinder head, fisheye endoscope and the two side endoscopes. Specifically, cylinder head presents a maximum temperature of 372 °C, located between the fisheye and the spark plug; slightly lower temperatures are instead reached in the area between the fisheye and one of the two intake valves, while the areas surrounding the endoscopes are not particularly thermally stressed. Also appreciable in figure 37b and 37c is the thermal field at the exhaust gas ejection port.
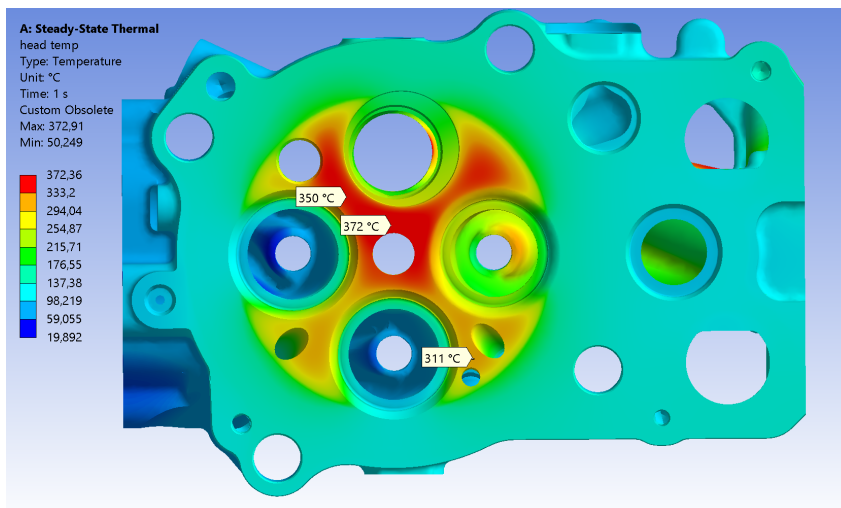
(a) Bottom view
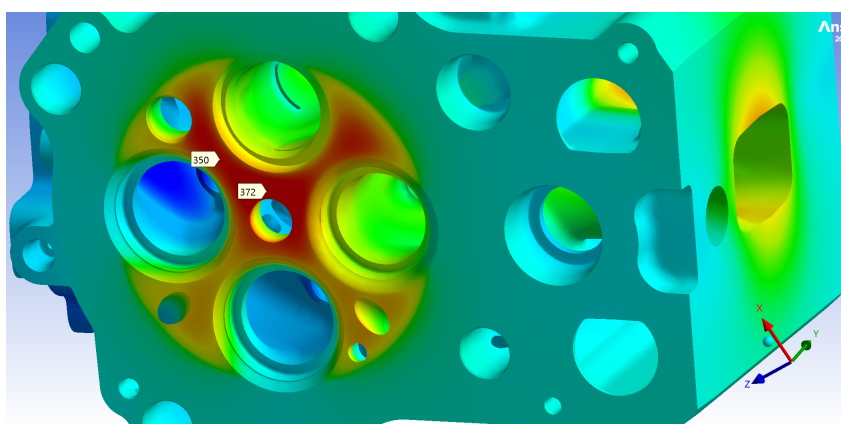
(b) Bottom and outlet
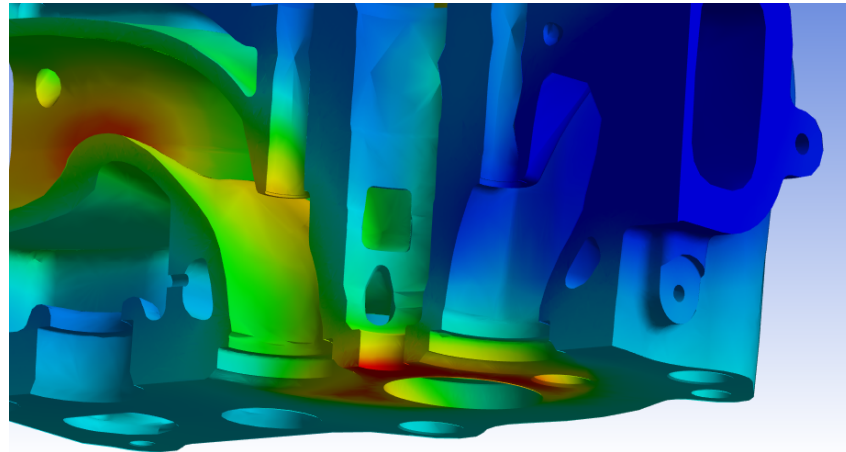
(c) Section view

Figure 37 Cylinder head thermal field
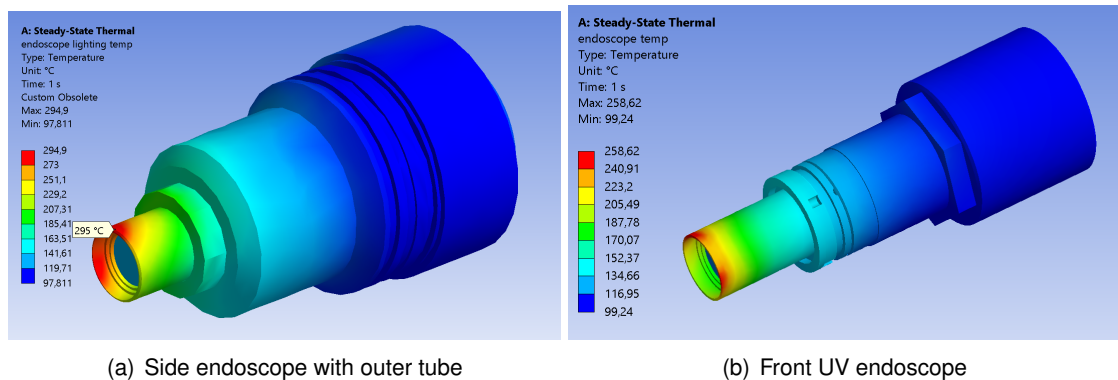
(a) Side endoscope with outer tube

(b) Front UV endoscope

Figure 39 Side endoscopes thermal field

The two side endoscopes are subject to a very uniform temperature distribution, going from the hotter zones around the combustion chamber to colder zones moving away from the head. It is possible to notice, especially in the endoscope with the outer tube, the temperature lowering effect given by the cooling system. the designed architecture is, among other things, ideal for the area where the optical apparatus is located, in fact, since the area near the exhaust valves is particularly heavy from the thermal point of view, the heat removal is greater than in the case of the endoscope screwed directly into the cylinder head. It is possible to validate this assertion by inserting a reaction probe in the simulation software at the areas of application of the boundary conditions for the two endoscopes; as in fact shown in table 10 the thermal power (negative because heat is removed from the components) is greater in absolute value in the case of the architecture with the outer tube.

(d) 3D view

(e) Section view
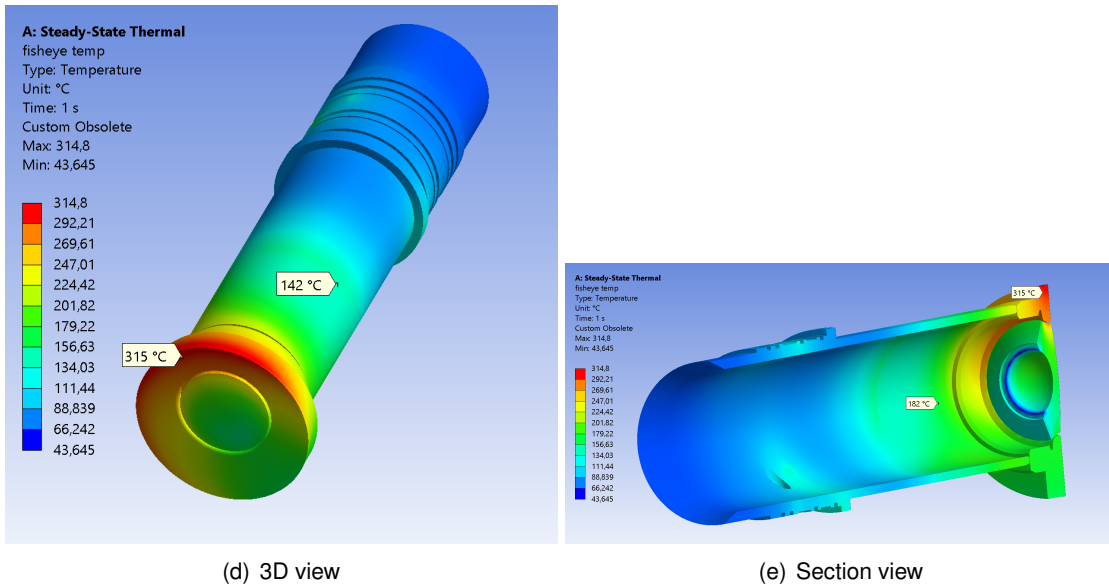
Figure 38 Fisheye endoscope thermal field

Component	Thermal power
Endoscope with outer tube	-1065 W
Directly screwed endoscope	-622 W
Fisheye endoscope	-1341 W

Table 10 Endoscopes cooling power

Moreover, the side endoscope with the outer tube shows to be more stressed than the front endoscope: this is mainly because of its positioning, being closer to the exhaust ducts and so presenting higher temperatures. Looking at Lavision datasheet (see Appendix A), endoscopes are capable of withstanding temperatures up to 200 °C, a limit that has been largely exceeded in this simulation. Same speech applies to the fisheye endoscope, which features a peak temperature of 315 °C and is therefore in crucial conditions with regard to thermal resistance prescribed by the manufacturer. These high temperatures mainly come from the combustion process that takes place cyclically in the combustion chamber, in addition to the exhaust gas ducts. Thus, if one intends to monitor combustion phenomena for prolonged times, the endoscopes used may not sustain the thermal loads to which they are subjected. However, it would be possible to improve the situation by installing alternative cooling systems, perhaps making use of cooling liquids rather than air. This would raise convective heat transfer coefficients by as much as an order of magnitude (to a first approximation), greatly reducing the temperatures reached during operation. Exposure to such temperatures for long periods of time should be avoided in any case, on risk of damaging the equipment and the delicate lens system inside it, being the same lenses held together by a special glue.

It should not be forgotten, however, that this simulation, being steady-state, poses a worst-

case scenario: in fact, the components are assumed to be exposed to these thermal fields until the transients are extinguished, which may not be the case for this application, especially if one is dealing with abnormal combustion phenomena that allow the engine to operate only for short periods of time under overloaded conditions. Thus, it can be asserted that obtained thermal fields may be critical if the fired operation is maintained for as long as it takes to reach a steady-state condition. Different discussion, on the other hand, concerns the final version of the engine, which lacks the openings for the optical equipment: energy production in the steady-state environment requires the power unit to operate for long periods of time, thus allowing the extinction of thermal transients and making the current analysis significantly more accurate.

5.2. Mechanical simulation results

In the following, main results regarding purely structural analysis are shown. Therefore, the results of the simulations below do not take into account the effect of thermal expansion of materials with temperature, an aspect that will be taken into account below. Figures are presented according to increasing load steps, as described in section 4.4.
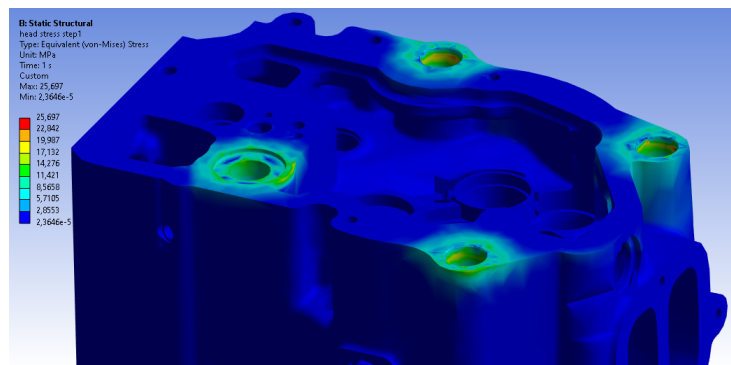
(a) Load step 1
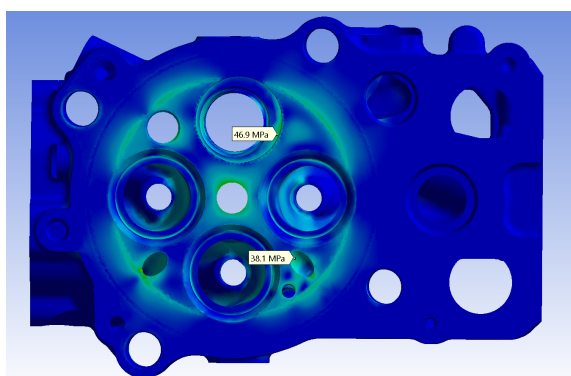
(b) Load step 2
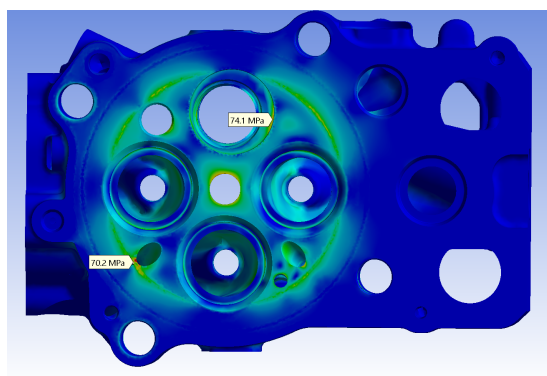
(c) Load step 3

Figure 40 Cylinder head mechanical stresses

After the application of the first load step, figure 40a shows that most of the initial stress is

coming from the contact pressure applied from the nuts to the four cylindrical surfaces on the head. Load steps 2 and 3 feature an increasing degree of stress, especially around the endoscope bores and the surface between the fisheye and the only exhaust valve present. In general, in the three cases there is an intensification effect of stresses at edges and areas that are particularly small and difficult to mesh; this may not be due to stresses actually present but simply to a numerics problem, which emerges when the solver works out the mathematical model.

(a) Load step 1

(b) Load step 2

(c) Load step 3
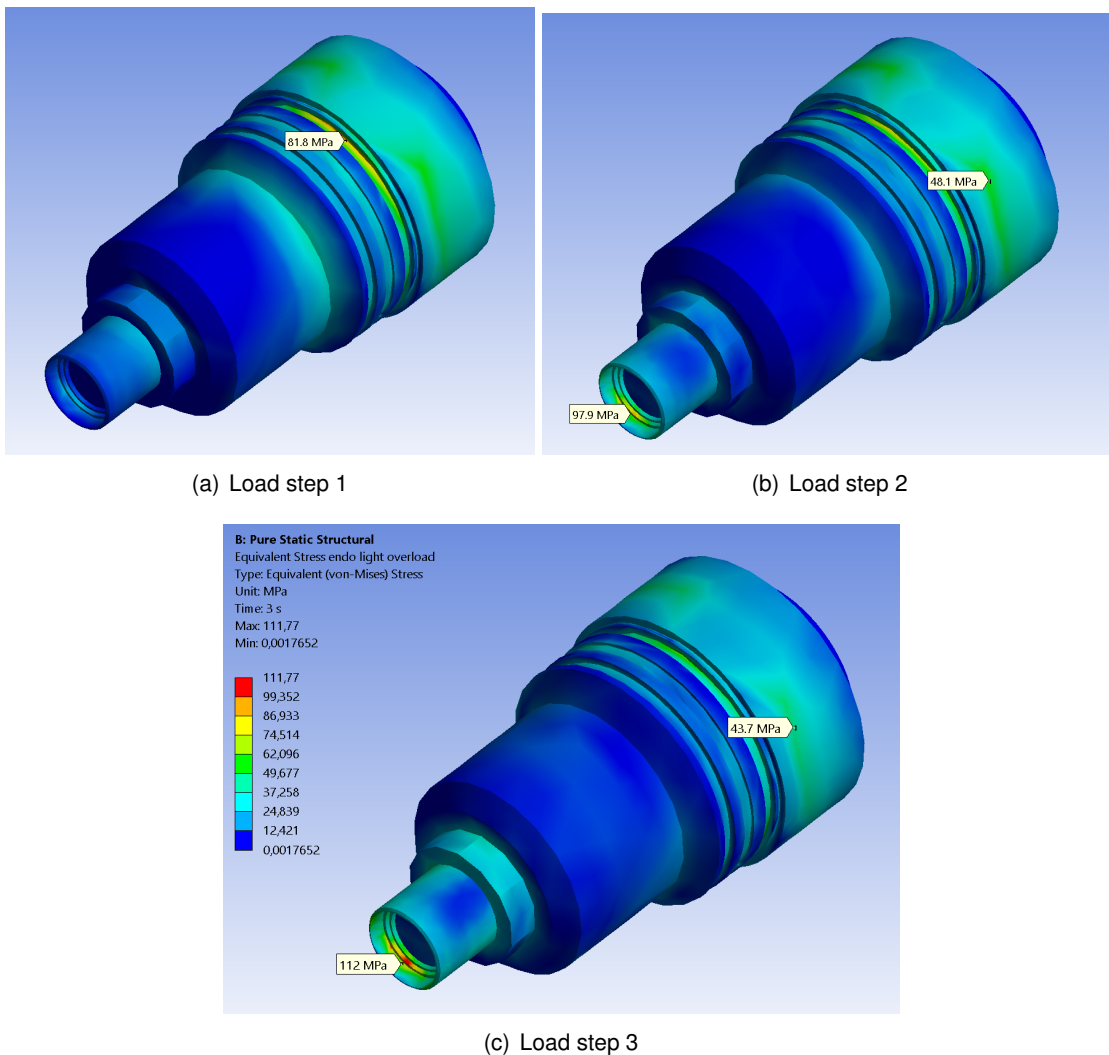
Figure 41 Endoscope lighting mechanical stresses

Lateral endoscopes, on the other hand, exhibit localized stresses near the combustion chamber area and partly on the cylindrical surface where the threaded connection occurs, especially for the lighting endoscope (figure 41). The application of the various load steps also shows two significant aspects: on the one hand, the intensification of stress near the endoscope tip, due to the increase of pressure up to the overload condition, and on the other hand, a progressive reduction of the pretension force is shown, due precisely to the pressure inside the combustion chamber that tends to push the endoscopes outward.
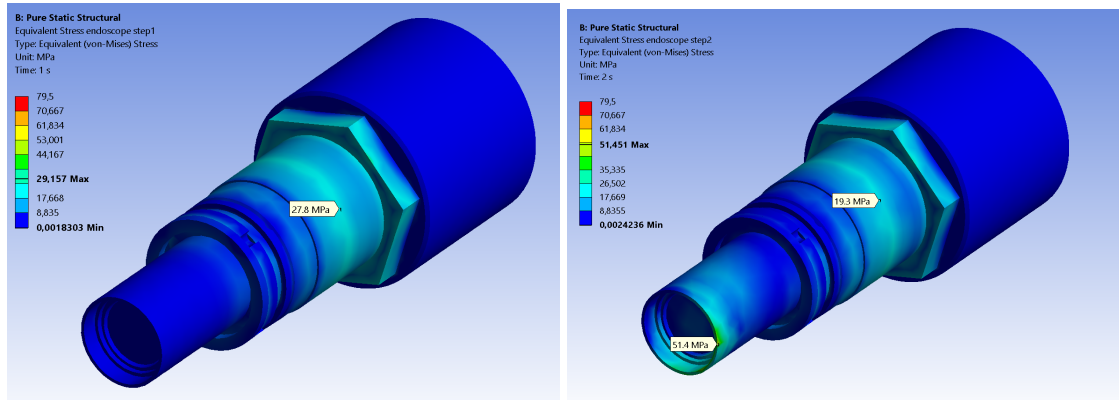
(a) Load step 1

(b) Load step 2
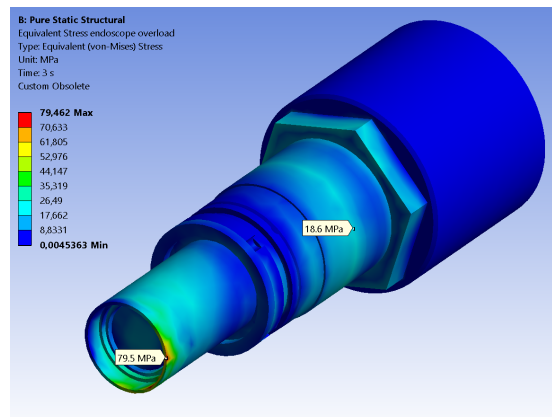
(c) Load step 3

Figure 42 UV endoscope mechanical stresses

(a) Load step 1

(b) Load step 2

(c) Load step 3
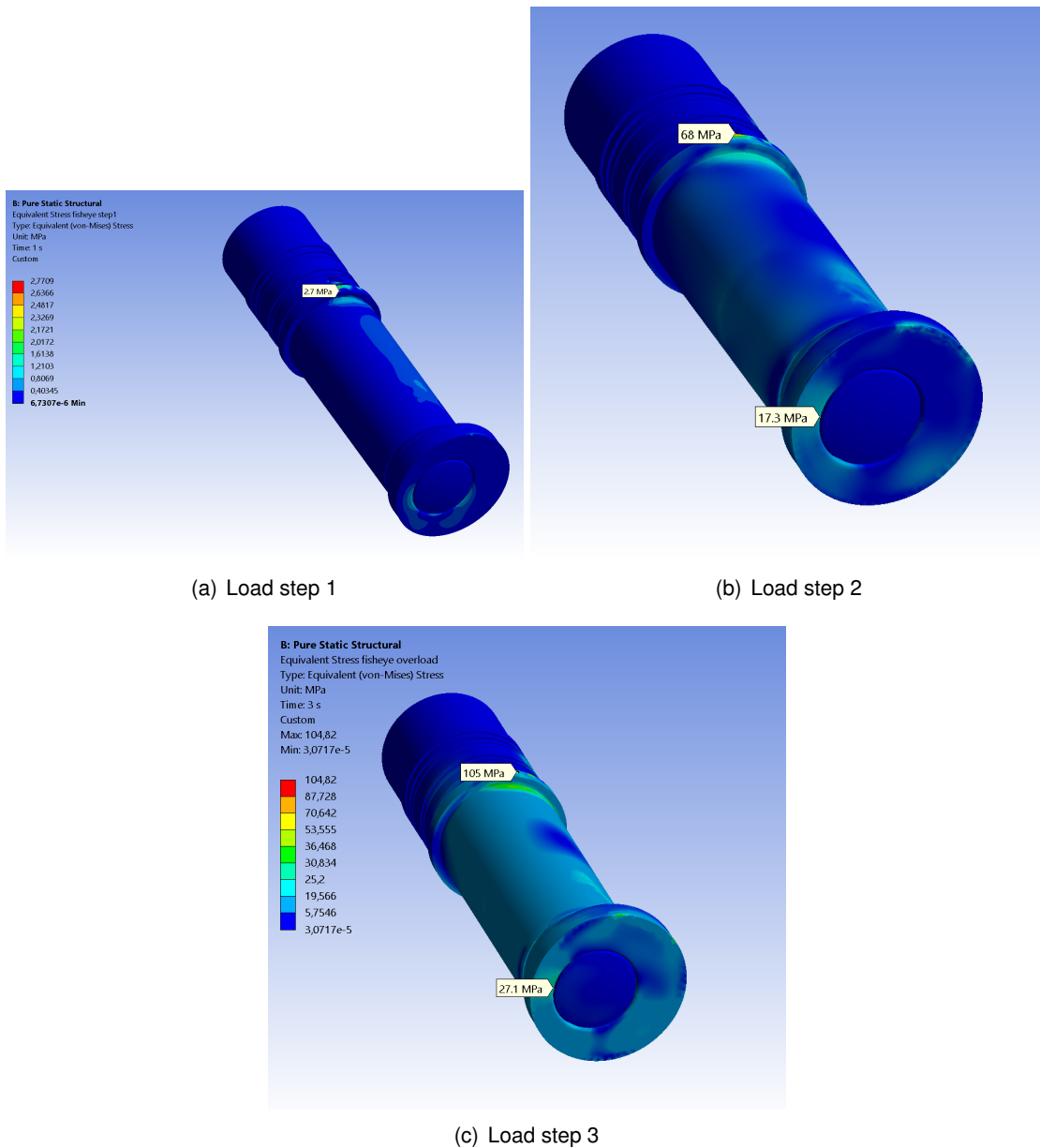
Figure 43 Fisheye mechanical stresses

Lastly, the fisheye endoscope appears to be the least stressed, with the maximum stress values reached in the interface area with the cylinder head. Although the mesh made has been extremely refined during the development of the model, this aspect may be due to geometric singularities present in the CAD model, or to an incorrect contact interface between the two components. Overall, the reduced stress range can be justified by the boundary conditions applied to the fisheye: since the location and connection in the cylinder head has not yet been designed, the only effects on stress are given by the contact between the parts and not by a real boundary condition (e.g., pre-tensioning) as in the case of the two side endoscopes.

5.2.1. Plates mechanical simulation

The proposed modified layout, involves reducing the thickness of the crankcase cover plate and valve train cover plate against an increase in the size of the cylinder head. Therefore, in order to conduct as thorough an analysis as possible, it is necessary to simulate the mechanical behaviour of these two plates as well, to verify that they do not reach the material yield strength limit conditions at any point. The results of the simulations are shown in Figures 44 and 45.
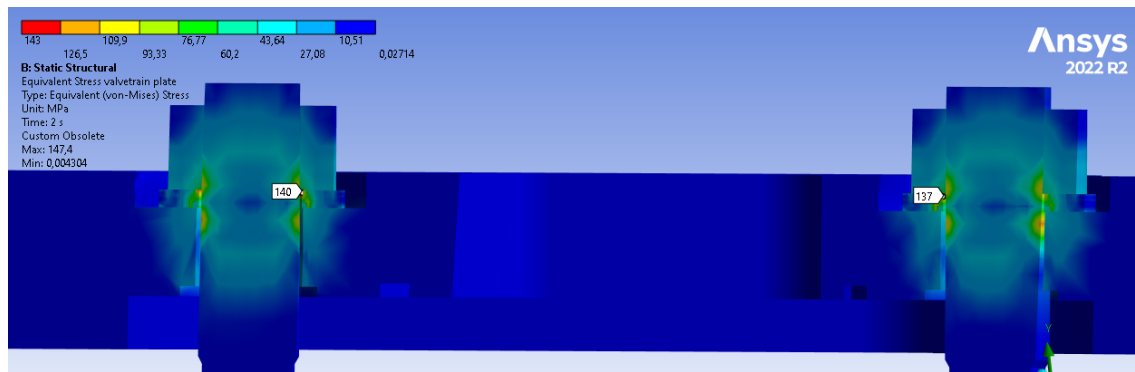
Figure 44 Bottom valve train cover plate stress field
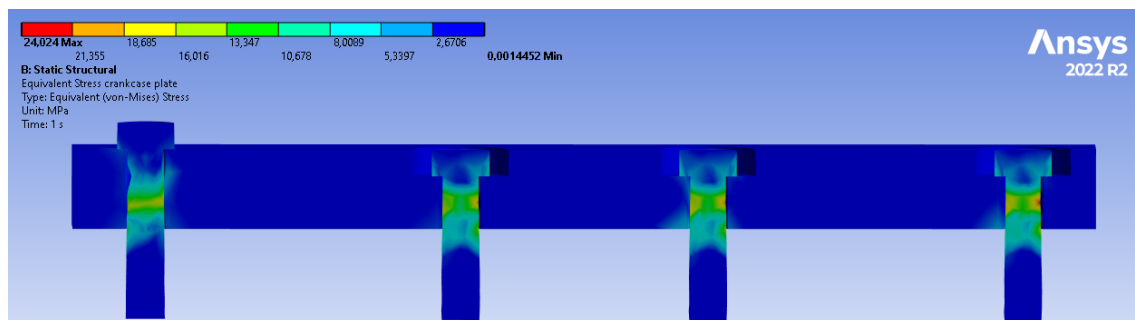
Figure 45 Top crank case cover plate stress field

As expected, the valve train cover is the most stressed of the two plates, being subject to the high static load coming from the tightening torque of the head bolts. The crank case cover definitely is not a critical component, with a maximum stress value of only 24 MPa. In conclusion, since the two plates do not have stresses approaching the yield strength limit of S355 steel and are also not exposed to large thermal fields, the problem of having to perform a thermomechanical simulation does not arise, and it can be assumed that they are statically verified for the loads they are subjected to.

5.3. Coupled thermo-mechanical simulation

After conducting a decoupled analysis, first thermal and then structural, it may be of considerable interest, especially in the context of ICEs, to conduct a thermo-mechanical simulation. Operationally, this involves solving the thermal model seen earlier, but using the results obtained (i.e., the temperature field) as boundary conditions for the structural problem. On the software side, the implementation of such a model was accomplished by duplicating the "static structural" block and linking to it the solution of the thermal problem in the setup sub-block, as shown in Figure 46.

Figure 46 Setting up a thermo-structural analysis in ANSYS

5.3.1. Cylinder head

(a) Load step 2

(b) Load step 3
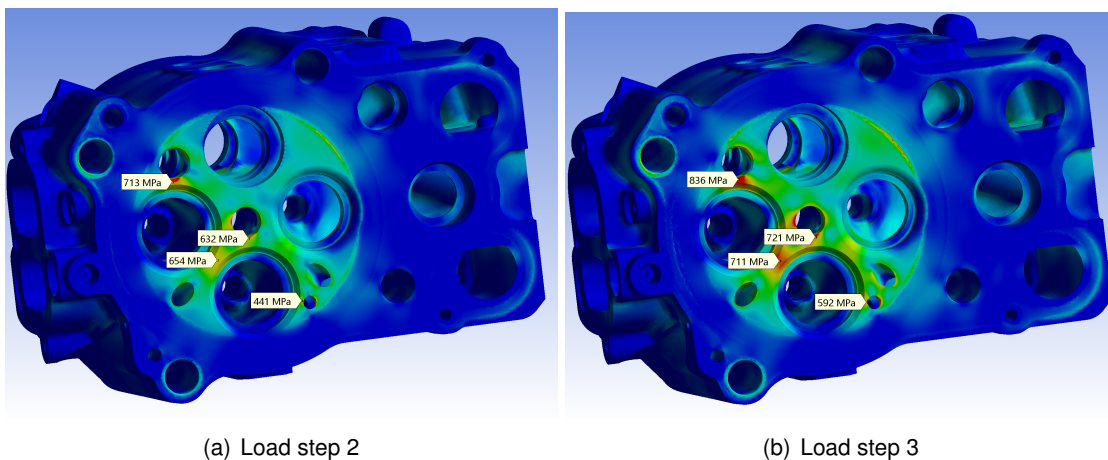
Figure 47 Cylinder head thermo-structural analysis

Figures 47a and 47b depict the mechanical behaviour of the head when normal operating pressure and overload pressure are applied, respectively. The temperature field has an extremely negative influence on stresses, as they have increased a lot from the purely mechanical simulation. Maximum values are above 800 MPa, which is also above the limit of compression strength of cast iron. In addition, the reduced thickness of the material in the areas of greatest stress only intensifies the stresses. It must be kept in mind, however, that those represented here are limiting situations, reached for extremely limited times and due to special circumstances (i.e. combustion anomalies). However, it remains necessary to check the component to avoid possible failure, which will be presented in the next chapter.

5.3.2. Endoscopes

(a) Load step 2   (b) Load step 3
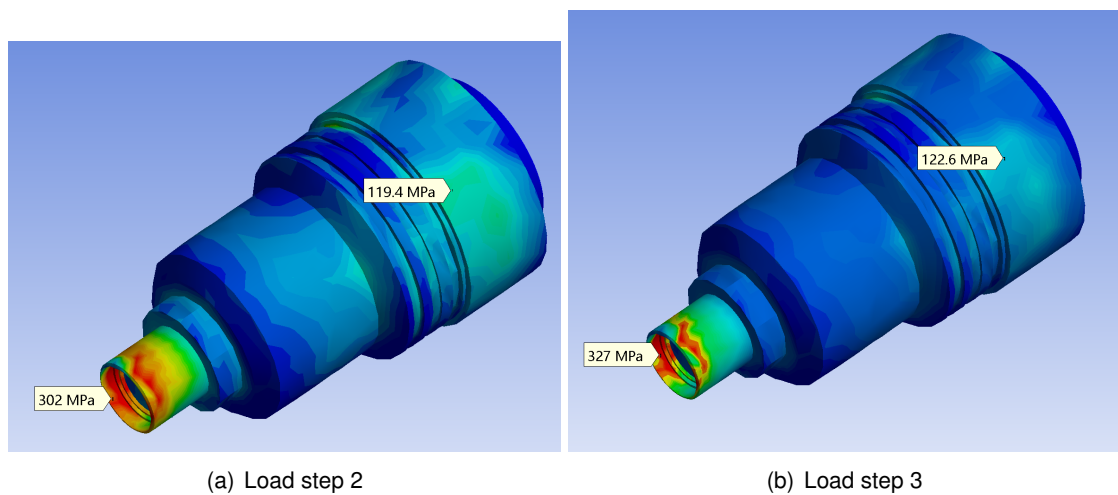
Figure 48 Cylinder head thermo-structural analysis

(a) Load step 2   (b) Load step 3
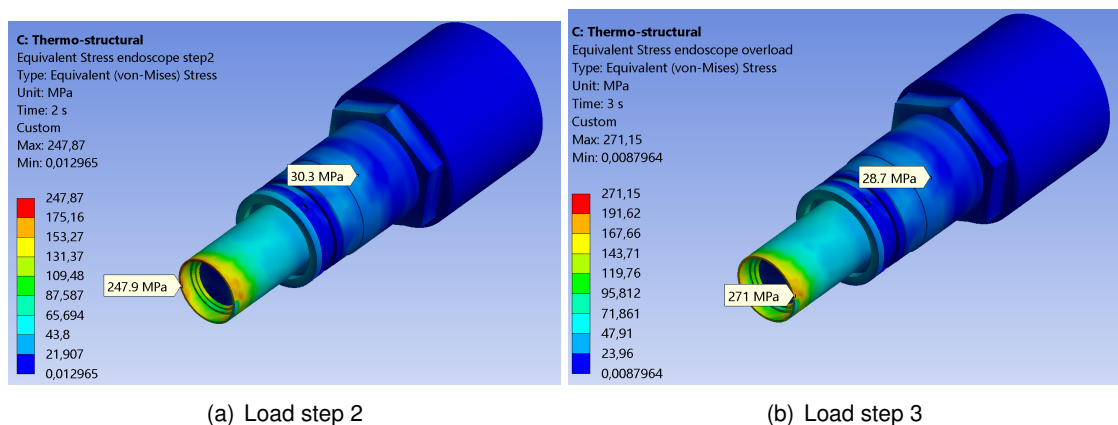
Figure 49 Cylinder head thermo-structural analysis

The lateral endoscopes (figures 48 and 49) exhibit an amplified stress range compared with purely mechanical simulation, and similarly, the loss of pretensioning of the threaded connection is noted. The fisheye instead presents a critical zone situated at the interface between the lens and the metal support, reaching a peak stress of 372 MPa, while the singular zone on the outer tube continues to be present.

(a) Load step 2   (b) Load step 3
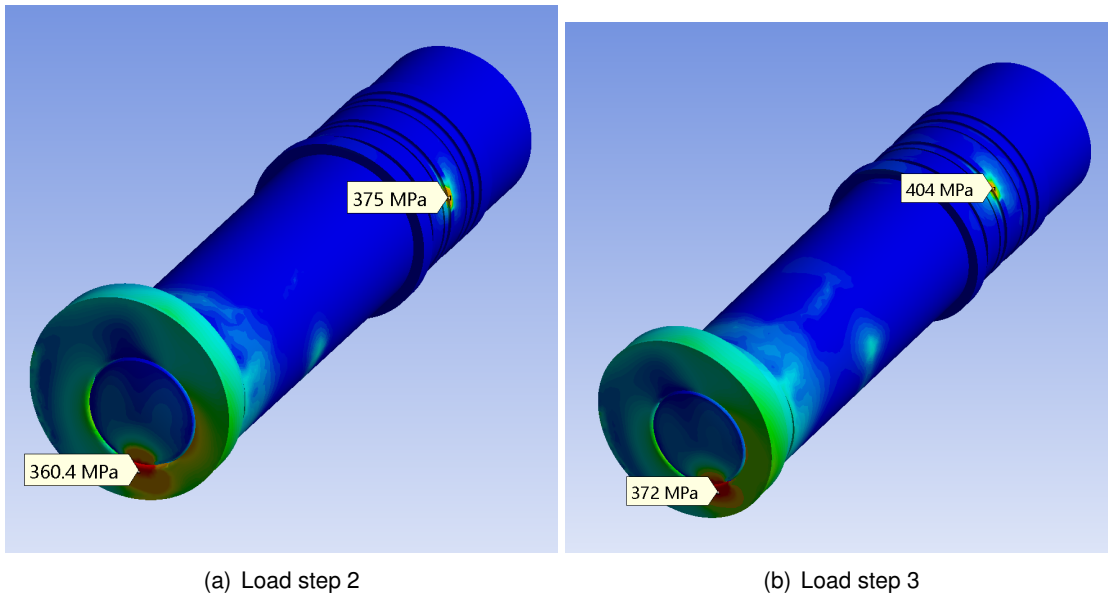
Figure 50 Cylinder head thermo-structural analysis

6. Analysis of Results

In this chapter we proceed to determine the effect of the stresses calculated in the previous chapter through simulations. To obtain results that are as reliable as possible, use will be made of the FKM standard [21], which is the fundamental guideline for the verification of any mechanical component. The following sections will take into account a static proof of strength first, then moving on to a fatigue safety assessment. The methodology used is also similar to that presented in [23] and [26], with appropriate adaptations to the specific case under consideration.

6.1. General considerations

FKM Guideline [21] prescribes to follow a step-by-step methodology, presented in general terms in the following flowchart:
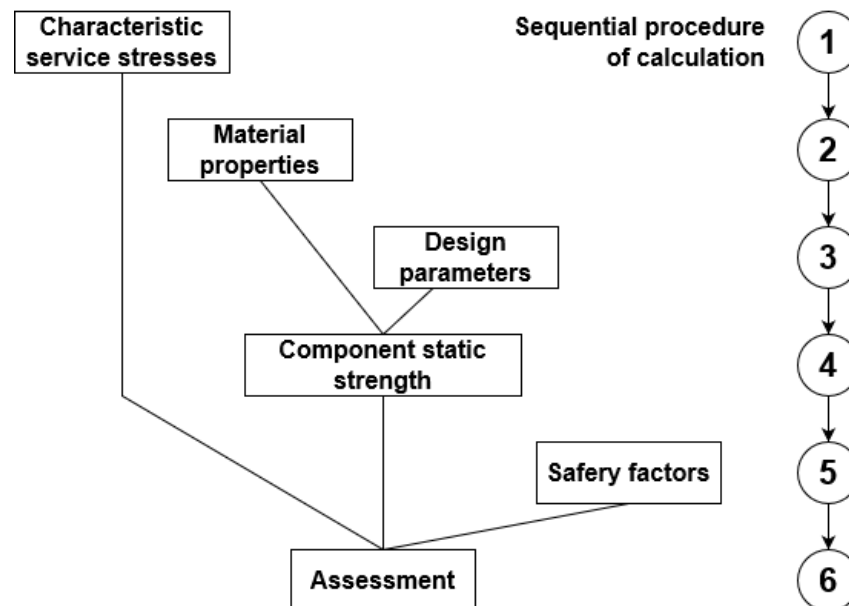
Figure 51 Static proof of strength methodology [21]

At the assessment stage, the characteristic values of service stress occurring in the component and the component strength values derived from mechanical material properties and design parameters are compared by including the required safety factors [21]. The same procedure is applied also to the fatigue stress assessment, taking into account the mean stress values and variable amplitude effects. The assessment provides the so-called degree of utilisation of the component: in order to have a safe operation under normal load conditions, this value has to be less than or equal to 1.

For reasons of space not all calculations are reported below; however, the coefficients and corrective factors and their influence on the final results are explained for each step.

6.2. Cylinder head static strength assessment

6.2.1. Stress values

	Position	Stress values during normal operation [MPa]			Local temperatures [°C]
		σ_1	σ_2	σ_3	
Zone 1	Between fuel injector and intake valve	-17,6	-320,3	-730,6	290 °C
Zone 2	Between intake valves	-28,5	-234,7	-682,5	284 °C
Zone 3	Around spark plug	-20,1	-451,9	-652,1	372 °C
Zone 4	Around endoscope lighting	-30,7	-276,3	-471,7	271 °C

Table 11 Cylinder head principal stress values and local temperatures

Table 11 shows, for each critical point, the principal stress components determined in the previous chapter (see figure 47), along with the local temperatures that will be used to perform a complete assessment of the component. Being the cylinder head made of a cast iron alloy (GJL-250), equivalent stress is determined using the normal stress hypothesis, typical for semi-ductile and brittle materials:

$$\sigma_{NH} = MAX|\bar{\sigma_1}|, |\bar{\sigma_2}|, |\bar{\sigma_3}| \tag{6.1}$$

every stress component $\bar{\sigma}_i$ is computed as:

$$\bar{\sigma}_i = \frac{\sigma_i}{f_{\sigma,i} \cdot K_{NL,i}} \tag{6.2}$$

where $f_{\sigma,i}$ is the compression strength factor, considered because of the tensile and compression strength difference, while $K_{NL,i}$ is the cast iron factor; their value will be determined in the following.

Since a multiaxial stress state is expected at the selected points, it is also interesting to calculate the degree of multiaxiality:

$$h = \frac{\sigma_h}{\sigma_\nu} \tag{6.3}$$

where σ_h is the hydrostatic stress, determined as follows:

$$\sigma_h = \frac{1}{3}(\sigma_1 + \sigma_2 + \sigma_3) \tag{6.4}$$

and $\sigma_\nu = \sigma_{NH}$.

6.2.2. Material properties

Here the nominal material properties are corrected with specific factors to take into account the differences between the test piece and the effective component. In particular, the following equations for both ultimate and yield tensile strength are used:

$$R_m = K_{d,m} \cdot K_A \cdot R_{m,N} \tag{6.5}$$

$$R_p = K_{d,p} \cdot K_A \cdot R_{p,N} \tag{6.6}$$

$R_{m,N}$ and $R_{p,N}$ are standard material properties taken from table 3. Coefficients $K_{d,m}$ and $K_{d,p}$ are called technological size factors, and they account for the decrease of the material strength values usually observed with increasing dimensions of the component [21]. In this case, the following equation is used for calculation:

$$K_{d,m} = K_{d,p} = 1.207 \cdot (d_{eff}/7.5mm)^{-0.1922} \tag{6.7}$$

where d_{eff} is the effective wall thickness of the cylinder head in the selected point.
Factor K_A is the anisotropy factor and for cast iron alloys such as GJL it can be set to 1 since the direction of the load application does not affect the material behavior.
Based on values provided in tables from the guideline [21], the compression strength factor is determined:

$$f_{\sigma,compr} = 2.5 \tag{6.8}$$

$$f_{\sigma,tens} = 1 \tag{6.9}$$

As previously determined, cylinder head is subjected to important thermal gradients; for this reason the temperature influence has to be considered in the definition of material properties. For temperatures above 100 °C, the guideline prescribes to calculate the temperature factors K_T as:

$$K_{T,m} = K_{T,p} = 1 - a_{T,m} \cdot (10^{-3}T/C)^2 \tag{6.10}$$

being the constant value $a_{T,m} = 1.6$ for GJL.

6.2.3. Design parameters

Now two other coefficients are considered:
the first one is n_{pl}: it accounts for load-bearing reserves once the elastic limit load has been exceeded [21]. Its calculation is performed with the application of the following equations:

$$\varepsilon_{ertr} = \begin{cases} \varepsilon_{ref} & \text{if } h \leq 1/3 \\ \varepsilon_0 + 0.3 \cdot (\frac{\varepsilon_{ref}-\varepsilon_0}{0.3})^{3h} & \text{if } h > 1/3 \end{cases} \tag{6.11}$$

where:

$$\varepsilon_0 = \frac{R_p}{E} \tag{6.12}$$

$$\varepsilon_{ref} = 0.4 \cdot A \tag{6.13}$$

being A the elongation at break of the material.

An additional factor called notch factor is then calculated as:

$$K_P = \frac{2 \cdot f_\sigma}{1 + f_\sigma} \tag{6.14}$$

Now the n_{pl} coefficient can finally be evaluated:

$$n_{pl} = MIN\left\{ E \cdot \frac{\varepsilon_{ertr}}{R_p}; K_P \right\} \tag{6.15}$$

Lastly, the cast iron coefficient is defined from the tables in the guideline:

$$K_{NL,tension} = 1.10 \tag{6.16}$$

$$K_{NL,compression} = 0.91 \tag{6.17}$$

6.2.4. Component strength

After the previous calculations, the final value of the component strength is computed as:

$$\sigma_{SK} = n_{pl} \cdot R_m \tag{6.18}$$

6.2.5. Safety factors

The definition of the overall safety factor goes through the determination of some individual factors. Going into detail, the most important factors to consider regarding cast iron are:

- j_m: assessment of fracture in the case of normal or short-term elevated temperatures, i.e. assessment of the tensile strength R_m or the strength at elevated temperature $R_{m,t}$

- j_{mt}: assessment of fracture in the case of long-term elevated temperatures, i.e. assessment of the creep strength $R_{m,Tt}$

These two factors are determined considering a mean probability of occurrence of the stresses, considering the operating point of the engine, and a mean entity of consequences in case of failure, being the whole system a research test bench and for this reason continuously subject to inspections. One has:

$$j_m = 1.8 \tag{6.19}$$

$$j_{mt} = 1.4 \tag{6.20}$$

Additional factors include also: j_G, whose value is set to 1.25 for castings that have been subject to non-destructive testing and a safety term specific for non-ductile cast components:

$$\Delta j = 0.5 - \sqrt{A/24\%} \tag{6.21}$$

The overall safety factor is then calculated with the following formula:

$$j_{ges} = j_G \cdot MAX\left\{\frac{j_m}{K_{T,m}}; \frac{j_m,t}{K_{Tt,m}}\right\} + \Delta j \qquad (6.22)$$

6.2.6. Static strength assessment

Finally, the degree of utilisation of the component can be calculated:

$$a_{SK} = \frac{\sigma_\nu}{\sigma_{SK}/j_{ges}} \qquad (6.23)$$

Table 12 shows the degree of utilization of the cylinder head in the selected areas of interest (see table 11 for zones):

	Zone 1	Zone 2	Zone 3	Zone 4
σ_ν [MPa]	321,1	299,9	286,6	207,4
σ_{SK} [MPa]	1200,0			
j_{ges}	3,45	3,44	3,74	3,40
a_{SK}	0,77	0,75	0,72	0,68

Table 12 Cylinder head static assessment results

The obtained results highlight, for every selected point, a degree of utilization which is less than 1. This means that the component is able to withstand the mechanical and thermal loads to which it is subjected from a static point of view. It should be noted, however, that the margin with respect to the unit value of the degree of use is definitely small, especially for the first three zones; in the case where the cylinder head is subjected to overload conditions, as in fact was simulated, the risk of static failure becomes more important, especially at those points where the thickness of the material is reduced (e.g. lateral and top boreholes for the endoscopes). Considering the overload condition of 400 bars peak in-chamber pressure, the utilization coefficients approach the unit, thus determining borderline conditions from the point of view of the static strength of the component.

6.3. Cylinder head fatigue strength assessment

For completeness of discussion, it was also decided to perform a fatigue assessment for the modified engine head; the purpose of this proof is to determine the number of stress cycles such that component failure occurs [21]. In order to perform this verification, an appropriate stress spectrum in terms of medium and alternate stresses has to be specified. In particular, the medium stress σ_m is given by the tensioning from the head bolts, the screw connection of the endoscopes, the press fit for the valves and the temperature field present in the component. The alternate stress component σ_a is instead given exclusively by the pressure in the combustion chamber, which varies cyclically from a zero value to the peak value, set in the previous chapter at a maximum of 250 bar during normal operative conditions. As specified in the FKM guideline, the procedure is structured as depicted in figure 52 and is applicable for a number of cycles greater than 10^4; for the set rotational speed of the engine of 1500 rpm, considering that peak load conditions are reached every two complete rotations of the crankshaft, this results in approximately 13 minutes of continuous operation, which is a relatively small period of time. However, given that the purpose of the test bench is to investigate abnormal combustion caused by the use of hydrogen, one is not expecting to deal with extremely long periods of fired operation, which makes the subsequent analysis acceptably reliable.
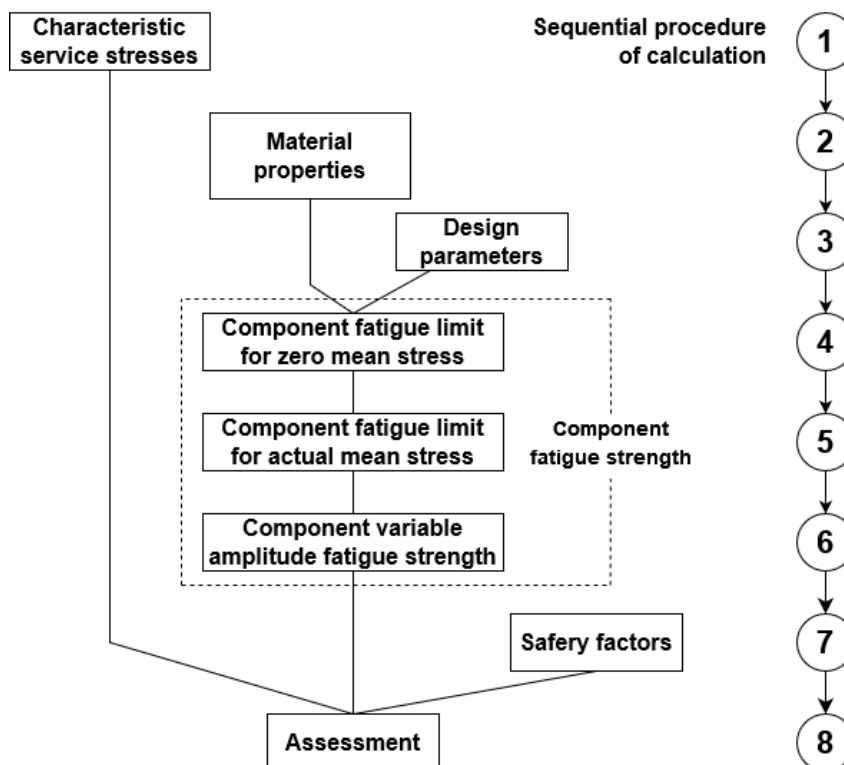
Figure 52 Fatigue proof of strength methodology [21]

Again, to avoid being too verbose in the discussion, the complete calculations are given in the Appendix. However, a full explanation of the necessary parameters to be determined in addition to the results obtained will be given below.

6.3.1. Characteristic service stresses

For block shaped 3D non-welded components, local principal stresses are taken into consideration [21]; first, the equivalent stress for each point is computed following the same criteria used during static strength assessment, then the two parameters of the stress spectrum are calculated as follows:

$$\sigma_a = \frac{\sigma_{max} - \sigma_{min}}{2} \tag{6.24}$$

$$\sigma_m = \frac{\sigma_{max} + \sigma_{min}}{2} \tag{6.25}$$
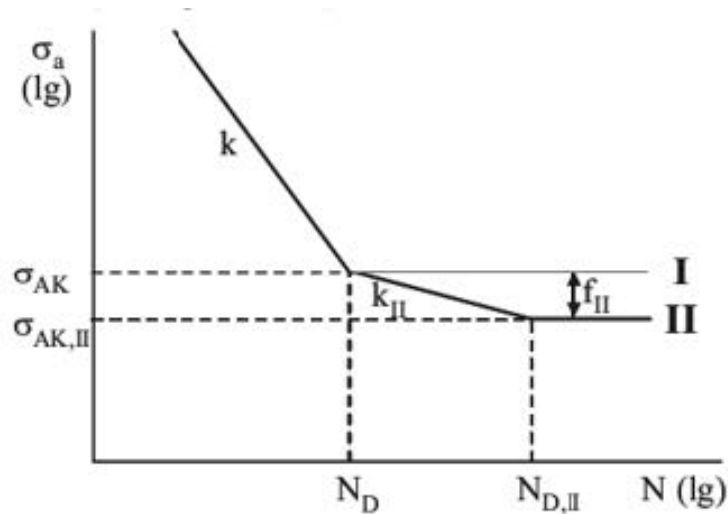
Figure 53 S-N curve models [21]

When one has to deal with fatigue stress, the S-N curve has to be defined; S-N curve is a curve represented in a bi-logarithmic diagram which describes the relationship between stress amplitude and the critical number of load cycles that lead the component to premature failure. In this case, model I is used (figure 53), with a characteristic that exhibits a knee and then a flat profile for $N > N_D$. This means that if the stresses are below the critical value σ_{AK} the component is fatigue-tested for a potentially infinite number of cycles; conversely, if the magnitude of stress is greater, early failure could occur. The number of working cycles is given in this case by the intersection of a horizontal line with the slope line k on the diagram in figure 53.

6.3.2. Material properties

The standard component values for a completely reversed axial stress is computed as:

$$\sigma_{W,zd} = f_{W,\sigma} \cdot R_m \tag{6.26}$$

where the parameter $f_{W,\sigma}$ is equal to 0.34 for GJL cast iron. Because of the S-N model used, it also represents the fatigue limit for $N = \infty$. The value $\sigma_{W,zd}$ applies to a number of cycles equal to 10^6.

6.3.3. Temperature factors

Temperature factor accounts for the reduction of fatigue limit of the material with increasing temperature [21]. The guideline distinguishes between normal, medium and high temperatures; in this case (T>100 °C) the following formula has to be used:

$$K_{T,D} = 1 - a_{T,D} \cdot (10^{-3} \cdot T/C)^2 \tag{6.27}$$

where $a_{T,D}$ equals to 1 for GJL.

6.3.4. Design parameters

A specific design factor for non-welded components has to be computed as follows:

$$K_{WK,\sigma} = \frac{1}{n_\sigma} \cdot \left(1 + \frac{1}{K_F} \cdot \left(\frac{1}{K_{R,\sigma}} - 1\right)\right) \cdot \frac{1}{K_V \cdot K_S \cdot K_{NL,E}} \tag{6.28}$$

where:

- n_σ is calculated considering the stress gradient normal to the direction of stress;

- K_F is the fatigue notch factor, which can be assumed to be equal to 1 for GJL;

- $K_{R,\sigma}$ considers the surface roughness;

- K_V is the surface treatment factor (equal to 1 in this case, since there is no surface treatment);

- K_S refers to the coating condition of the component;

- $K_{NL,E}$ is a constant value for GJL that accounts for the non-linear elastic strain behaviour of the material; in this case this coefficient values 1,05.

6.3.5. Component strength

As for the component fatigue strength, two different cases have to be distinguished: fatigue limit for reversed stress (without the influence of mean stress) and fatigue limit considering the influence of mean stress factor.

The fatigue limit without mean stress influence is simply computed reducing the fatigue value previously computed by the K_{WK} factor, that accounts for all design parameters.

$$\sigma_{WK} = \frac{\sigma_{W,zd}}{K_{WK}} \tag{6.29}$$

If the influence of mean stress is considered, the amplitude of the component fatigue strength is calculated depending on the given mean stress, considering a multiaxial state of stress [26]. This involves the calculation of a new coefficient K_{AK}, whose value depends on the stress ratio R, defined as:

$$R = \frac{\sigma_{min}}{\sigma_{max}} \tag{6.30}$$

For every selected point, each of which is characterized by three principal stresses and consequently by different stress ratios, the coefficient $K_A K$ is computed. For detailed calculations one can refer to the material provided in the Appendix A.

6.3.6. Safety factors

Safety factors calculated with this procedure are valid on the condition that characteristic strength values exhibit an average probability of survival of 97,5% [26]. This determines the value of the partial safety factor j_S to be 1.

Total safety factor j_D is then determined as:

$$j_D = \frac{j_S \cdot j_F \cdot j_G}{K_T, D}$$ (6.31)

where j_F considers the non-destructive testing performed on the cast material (same coefficient used in static strength assessment), j_G accounts for the consequences of failure for the component and K_T, D is the temperature factor already seen before.

Moreover, the guideline prescribes to increase the value of the safety factor by a quantity Δj defined as:

$$\Delta j = 0,5 - \sqrt{A/50\%}$$ (6.32)

to take in consideration the brittle nature of GJL cast iron.

6.3.7. Fatigue strength assessment

Finally, the fatigue strength assessment is accomplished for each stress component, with the following formula:

$$a_{BK,\sigma} = \frac{\sigma_{a,i}}{\sigma_{BK}/j_D} \leq 1$$ (6.33)

For detailed calculations of the various coefficients, the reader may refer to the tables in Appendix A.

Table 13 shows the results for the computed safety factors for the four zones previously selected, highlighting a definitely non-critical fatigue stress situation during normal engine operative conditions. Such low values of the material utilization coefficients are justified by the fact that the overall stress state in the most stressed areas is compressive; since GJL cast iron has high compressive strength, the material choice is ideal for the technological application because it poses no special problems from the standpoint of fatigue strength. The occurrence of overload conditions, as displayed in the static assessment section, could lead in any case to premature failure and for this reason these must be of limited duration.

	Zone 1	Zone 2	Zone 3	Zone 4
a_{BK,σ_1} [MPa]	0,02	0,06	0,08	0,15
a_{BK,σ_2} [MPa]	0,22	0,28	0,21	0,28
a_{BK,σ_3} [MPa]	0,27	0,28	0,23	0,30

Table 13 Fatigue stress assessment for cylinder head

7. Outlook and Final Conclusion

The entire thesis work revolved around the test bed engine in use at the Chair of Sustainable Mobile Drivetrains at TUM. The use of hydrogen as a fuel in green power generation in stationary applications raises many issues, starting with the safety concern due to its high flammability and moving on to production and large-scale distribution. The main purpose of the test bench is to investigate the abnormal combustion phenomena affecting the air-hydrogen mixture: for this reason, the simulation analyses conducted were developed with a view to investigating the thermal and mechanical stress fields affecting the most stressed components, such as the engine head, upper and lower support plates and endoscopes. The housings for the latter, which are necessary for direct observation inside the combustion chamber, resulted in a general weakening of the cylinder head due to the boreholes drilled into it.

The approach followed for the simulation involved first performing a steady-state thermal analysis in order to calculate the temperatures in the components of interest and verifying that these did not exceed the limits imposed by the manufacturer, with particular regard to the optical equipment. Next, a structural simulation was carried out by applying the most significant boundary conditions on the assembly, identifying as the most stressed areas those present on the lower face of the cylinder head, as well as those in the vicinity of the optical endoscopes, with significant compressive stresses.

The two previous simulations were then joined in cascade, using the results of the thermal analysis as input inside the mechanical simulation, highlighting how stresses are significantly amplified by thermal expansion of the material. Following this, a complete stress assessment of the engine head was carried out following step by step the FKM standard, both from a static and fatigue point of view. The utilization factors of the component in the most stressed areas were found to be slightly less than one with regard to static strength, while they are significantly less than unity in the case of fatigue assessment. This aspect confirms that the design of the component is adequate to withstand the thermomechanical loads to which it is subjected; a simulation was also carried out for overload conditions, up to operating pressures in the combustion chamber of 400 bar, realistically determined by the back-firing and pre-ignition phenomena of the air-fuel mixture. It was observed that this boundary condition results in a general intensification of the stress field, especially in those areas where notches are present or material thickness is reduced. The results obtained from the simulation of some areas (cylinder head and fisheye structural simulation in particular) showed some stress peaks, probably excessive when compared to the real stresses of the components studied. These singularity conditions occurred in spite of the fact that a particularly fine mesh was made, evidencing that some geometric singularities are still present in the CAD model that are preventing reliable results from being achieved in some areas.

In any case, it should be pointed out that the powerplant studied must also be able to withstand these overload conditions, which are often voluntarily induced for very short periods of time in order to characterize the combustion process. It is therefore possible to assert how

the thermomechanical loads on the components of interest are certainly not negligible, but nevertheless do not pose a risk to their structural integrity for short ranges of operation. Going into much detail, thermal conditions reached at the endoscopes have shown to be critical, with temperatures being even 100 °C higher that the limit from the manufacturer. However, since the observation of abnormal combustion phenomena doesn't need extremely long fired operation times, one can assert that the research engine can withstand these continuous thermal loads for times of less than one hour. Structural-wise, normal chamber pressure of 250 bars doesn't seem to pose any risk for the integrity of the assembly, while consecutive cycles of operation in which the threshold pressure conditions (400 bars) are reached definitely pose a problem, showing a utilization factor that, at least from a static point of view, is around the unit value.

With a view to possible future developments, it would certainly be possible to implement an alternative and more accurate calculation of the thermal field with the realization of a CFD-type analysis from the experimental data collected on the test bench itself; in fact, in a more accurate thermal model the convective heat transfer coefficients for both the working fluids and the air in the cooling ducts of the optical equipment change from point to point in space, as well as changing as a function of time. This kind of simulation, among other things, directly influences the results of the thermostructural analysis and thus leads to more reliable estimates of the magnitude of mechanical stress present in the assembly. Ultimately, two additional suggestions may relate to the implementation of transient simulations, especially the start-up transient which for a large motor for stationary applications is particularly demanding and, last but not least, the complete design of the connection between fisheye endoscope and cylinder head, so as to determine the right positioning to limit stresses and ensure proper cooling of the component.

Bibliography

[1] *ANSYS ICEM CFD - Tutorial Manual*. 2007.

[2] Tomas Bartkowski et al. "Effects of Ambient Air Humidity on Emissions and Efficiency of Large-Bore Lean-Burn Otto Gas Engines in Development and Application". In: Aug. 2020. DOI: 10.1115/power2020-16572.

[3] Richard van Basshuysen and Fred Schäfer. SAE International, 2016. ISBN: 978-0-7680-8024-7. URL: https://app.knovel.com/hotlink/toc/id:kpICEHBC04/internal-combustion-engine/internal-combustion-engine.

[4] Sebastian Beil. *Simulation der thermischen und mechanischen Belastung des Zylinderkopfes eines Großgasmotors*. 2013.

[5] McKinsey & CO. *Hydrogen council*. McKinsey & CO, 2022.

[6] Karl-Heinz Decker. "Maschinenelemente: Funktion, Gestaltung und Berechnung". In: Hanser Fachbuchverlag, 2018.

[7] Stefan Eicheldinger et al. "Optical screening investigations of backfire in a large bore medium speed hydrogen engine". In: *International Journal of Engine Research* 23.5 (2022), pp. 893–906. DOI: 10.1177/14680874211053171. eprint: https://doi.org/10.1177/14680874211053171. URL: https://doi.org/10.1177/14680874211053171.

[8] P. V. Elumalai et al. "Hydrogen in Spark Ignition Engines". In: *Application of Clean Fuels in Combustion Engines*. Ed. by Gabriele Di Blasio et al. Singapore: Springer Nature Singapore, 2022, pp. 195–213. DOI: 10.1007/978-981-16-8751-8_10.

[9] P. V. Elumalai et al. "Hydrogen in Spark Ignition Engines". In: *Application of Clean Fuels in Combustion Engines*. Ed. by Gabriele Di Blasio et al. Singapore: Springer Nature Singapore, 2022, pp. 195–213. ISBN: 978-981-16-8751-8. DOI: 10.1007/978-981-16-8751-8_10. URL: https://doi.org/10.1007/978-981-16-8751-8_10.

[10] Udo Gerke. "Numerical analysis of mixture formation and combustion in a hydrogen direct-injection internal combustion engine". PhD thesis. ETH Zürich, 2007.

[11] Hygear. *Steam methane reforming*. URL: https://hygear.com/technologies/steam-methane-reforming/.

[12] Tehseen Johar and Chiu-Fan Hsieh. "Design Challenges in Hydrogen-Fueled Rotary Engine - A Review". In: *Energies* 16.2 (2023). ISSN: 1996-1073. DOI: 10.3390/en16020607. URL: https://www.mdpi.com/1996-1073/16/2/607.

[13] Stephan Karmann et al. "Optical and Thermodynamic Investigations of a Methane-and Hydrogen-Blend-Fueled Large-Bore Engine Using a Fisheye Optical System". In: *Energies* 16.4 (2023). ISSN: 1996-1073. DOI: 10.3390/en16041590. URL: https://www.mdpi.com/1996-1073/16/4/1590.

[14] Jörg Kempf. *Pumps Pass Endurance Test in Pressurised Coal Gasification Process*. 2011.

[15] Manfred Klell, Helmut Eichlseder, and Alexander Trattner. "Hydrogen in Automotive Engineering". In: Springer Wiesbaden, 2022. Chap. Storage and Transport.

[16] Rainer Kurz et al. "Chapter 6 - Transport and storage". In: *Machinery and Energy Systems for the Hydrogen Economy*. Ed. by Klaus Brun and Timothy Allison. Elsevier, 2022, pp. 215–249. ISBN: 978-0-323-90394-3. DOI: `https://doi.org/10.1016/B978-0-323-90394-3.00003-5`. URL: `https://www.sciencedirect.com/science/article/pii/B9780323903943000035`.

[17] LaVision. *Endoscopic imaging*.

[18] Ronald List. *CATIA V5 - Grundkurs für Maschinenbauer*. Springer Vieweg Wiesbaden, 2015. DOI: `https://doi.org/10.1007/978-3-658-07822-5`.

[19] Yao Liu et al. "Quantitative Measurement of OH* and CH* Chemiluminescence in Jet Diffusion Flames". In: *ACS Omega* 5.26 (2020). PMID: 32656412, pp. 15922–15930. DOI: `10.1021/acsomega.0c01093`. eprint: `https://doi.org/10.1021/acsomega.0c01093`. URL: `https://doi.org/10.1021/acsomega.0c01093`.

[20] Yongtao Lyu. "Introduction". In: *Finite Element Method: Element Solutions*. Singapore: Springer Nature Singapore, 2022, pp. 1–18. ISBN: 978-981-19-3363-9. DOI: `10.1007/978-981-19-3363-9_1`. URL: `https://doi.org/10.1007/978-981-19-3363-9_1`.

[21] Forschungskuratorium Maschinenbau. "Fkm-Guideline : Analytical Strength Assessment of Components in Mechanical Engineering". In: 5th. English version ed. Frankfurt/Main: Forschungskuratorium Maschinenbau, 2003.

[22] Günter P. Merker and Rüdiger Teichmann. "Grundlagen Verbrennungsmotoren:Funktionsweise und alternative Antriebssysteme Verbrennung, Messtechnik und Simulation". In: Springer Vieweg Wiesbaden, 2018.

[23] Philip Müller. *Thermische und mechanische Festigkeitsberechung eines Zylinderkopfs für einen Otto-Forschungsmotor mit zentral angeordnetem Injektor*. 2013.

[24] *OHV vs. OHC configuration*. URL: `https://www.honda-engines-eu.com/en/`.

[25] A Onorati et al. "The role of hydrogen for future internal combustion engines". In: *International Journal of Engine Research* 23.4 (2022), pp. 529–540. DOI: `10.1177/14680874221081947`. eprint: `https://doi.org/10.1177/14680874221081947`. URL: `https://doi.org/10.1177/14680874221081947`.

[26] Hitesh Babubhai Patel. "Using MS Excel as solver in ansys workbench for the static and fatigue assessment in accordance with the FKM guideline". masterthesis. Hochschule Rhein-Waal, 2022, p. 172.

[27] Dr.-Ing. Maximilian Prager. "Hydrogen Mobility". 2022.

[28] Hannes Martin Röhrle. *Konstruktion eines Zylinderkopfs mit endoskopischem Brennraumzugang*. 2016.

[29]   Hannes Martin Röhrle. *Konstruktion eines Zylinderkopfs mit endoskopischem Brennraumzugang*. 2016.

[30]   Kostantin Semenov. *Dreamstime. Hydrogen Atom on White Background*.

[31]   Sumit Sood et al. "Generic Dynamical Model of PEM Electrolyser under Intermittent Sources". In: *Energies* 13.24 (2020). DOI: 10.3390/en13246556. URL: https://www.mdpi.com/1996-1073/13/24/6556.

[32]   E. Stefanelli. "Otto and Diesel cycle comparison". In: ().

[33]   Richard Trott and Ingo Friedrich. "Review of State of the Art and Future Options of Hydrogen Storage Systems for Internal Combustion Engines with Direct Fuel Injection for Use in Heavy Duty Vehicles". In: *21. Internationales Stuttgarter Symposium*. Ed. by Michael Bargende, Hans-Christian Reuss, and Andreas Wagner. Wiesbaden: Springer Fachmedien Wiesbaden, 2021, pp. 64–76. ISBN: 978-3-658-33521-2.

[34]   Adetokunboh T. Bakenne William J. Nuttall. "Fossil Fuel Hydrogen. Technical, Economic and Environmental Potential". In: Springer Cham, 2019.

[35]   Andreas Züttel. "Hydrogen storage methods". In: *Die Naturwissenschaften* 91 (Apr. 2004), pp. 157–72. DOI: 10.1007/s00114-004-0516-x.

A Appendix

	For Ultraviolet Light		
Part number	1108450	1108852	1108855
Description	UV camera endoscope 8 mm	UV high-efficiency endoscope (incl. optical sealing tube)	UV high temperature endoscope
Wavelenth	Optimized λ: 350 nm Usable λ: 248 - 550 nm	Optimized λ: 220 - 450 nm Usable λ: 200 - 750 nm	300 - 340 nm
Distal end diameter	8 mm	10 mm 12 mm (optical sealing tube)	38 mm
Effective length	25 mm(d= 8 mm) 260 mm (d= 15 mm)	24 mm (d= 10 mm) (variable)	1200 mm
Working distance	50 mm	35 mm	100 mm - ∞
Viewing direction	0° (straight)		0° (straight), 70° (adapter)
Opening angle	50°	>50°	40°
Max distal end temperature T	120 °C	200 °C	2000 °C
Pressure resistance (absolute)	1.5 bar	300 bar with included sealing insert	atmospheric
Camera mount	• M52 adapter • C-mount	• de-coupled lens F-mount	C-mount
Focus	Internal focus	via lens	Internal focus
Filter mount	1" and 2" filter holder	M52 filter thread	-
Relative transmission*	100 %	1000 %	N/A

Input data

			Notes:
Nominal diameter	42,000	mm	M42x2 8.8 class metric threaded connection
Mean diameter	40,493	mm	from tables
Core diameter	39,194	mm	" "
Inner diameter	32,600	mm	hollow section
Pitch	2,000	mm	
Friction coefficient	0,120		
E1	210000,000	MPa	Structural steel elastic modulus
E2	100500,000	MPa	GJL 250 elastic modulus
Lf	17,000	mm	length of threaded connection
Rm	800,000	MPa	
Rp02	640,000	MPa	yield strength of screw
alpha	0,524	rad	helix angle for metric thread
exploitation factor	0,115		fraction of Rp02

Calculations

S_core	550,753	mm^2	
dt	42,000	mm	subhead diameter
k	1,329		geometric factor
Fv_lim	**16,149**	**kN**	
Mt_lim	**91,139**	**Nm**	

External load (combustion chamber pressure)

p	250,000	bar
S_loaded	201,062	mm^2
F_ext	5026,548	N

		Zone 1	Zone 2	Zone 3	Zone 4
	Position	Between fuel injector and intake valve	Between 2 intake valves	Around spark plug	Around endoscope lighting
Input values	sigma 1 [MPa] sigma 2 [MPa] sigma 3 [MPa]	-17,6 -120,4 -180,9	-28,5 -134,6 -177	-20,1 -109,4 -157,2	-30,7 -134,4 -161,9
	Local material thickness [mm]	18	21	17	19
	Local temperatures [°C]	290	284	372	271
Stress values	sigma_1_signed [Mpa]	-7,7	-12,5	-8,8	-13,5
	sigma_2_signed [MPa]	-52,9	-59,2	-48,1	-59,1
	sigma_3_signed	-79,5	-77,8	-69,1	-71,2
	sigma_NH	79,5	77,8	69,1	71,2
	K_NL	0,91	0,91	0,91	0,91
	Hydrostatic stress sigma_h	-106,3	-113,4	-95,6	-109,0
Material properties	Kd,m = Kd,p	1,02	0,99	1,03	1,01
	f_sigma,compr	2,5	2,5	2,5	2,5
	f_sigma,tens	1	1	1	1
	K_T,m =K_T,p	0,87	0,87	0,78	0,88
	Degree of multiaxiality (h)	-1,34	-1,46	-1,38	-1,53
Design parameters	eps_crtr Kp n_pl	1,20E-02 1,429 1,43	1,20E-02 1,429 1,43	1,20E-02 1,429 1,43	1,20E-02 1,429 1,43
Component strength	sigma_sk [MPa]	357,1	357,1	357,1	357,1
Safety factors	j_m j_mt delta_j j_g j_ges	1,8 1,4 0,85 1,25 3,45	1,8 1,4 0,85 1,25 3,44	1,8 1,4 0,85 1,25 3,74	1,8 1,4 0,85 1,25 3,40
Static strength assessment	a_sk	**0,77**	**0,75**	**0,72**	**0,68**

			Zone 1	Zone 2	Zone 3	Zone 4
		Position	Between fuel injector and intake valve	Between 2 intake valves	Around spark plug	Around endoscope lighting
Input values	sigma_max (bolts + pressure)	sigma 1 [MPa]	-17,6	-28,5	-20,1	-30,7
		sigma 2 [MPa]	-120,4	-134,6	-109,4	-134,4
		sigma 3 [MPa]	-180,9	-177	-157,2	-161,9
	sigma_min (only bolts)	sigma 1 [MPa]	-11,8	-6,8	4,4	15,5
		sigma 2 [MPa]	-34,9	-27,2	-29,7	-30,8
		sigma 3 [MPa]	-76,8	-71	-67,3	-49,7
	Mean stress values	sigma_m1	-14,7	-17,65	-7,85	-7,6
		sigma_m2	-77,65	-80,9	-69,55	-82,6
		sigma_m3	-128,85	-124	-112,25	-105,8
	Alternate stress values	sigma_a1	-2,9	-10,85	-12,25	-23,1
		sigma_a2	-42,75	-53,7	-39,85	-51,8
		sigma_a3	-52,05	-53	-44,95	-56,1
	Local material thickness [mm]		18	21	17	19
	Local temperatures [°C]		290	284	372	271
Design parameters		G_sigma	0,7	0,68	0,74	0,62
		n_sigma	1,8	1,8	1,8	1,7
		K_t,D	0,92	0,92	0,86	0,93
		K_WK	0,5	0,5	0,5	0,5
		sigma_w,zd	77,9	78,1	73,2	78,8
zero mean stress		sigma_WK	145,8	145,5	138,9	143,7
Influence of mean stress	R (stress ratio)	sigma_min/sigma_max_1	0,67	0,24	-0,22	-0,50
		sigma_min/sigma_max_2	0,29	0,20	0,27	0,23
		sigma_min/sigma_max_3	0,42	0,40	0,43	0,31
	Mean stress sensitivity	M_sigma	0,5	0,5	0,5	0,5
	K_AK coefficients	K_AK_sigma1	0,52	0,61	0,50	0,50
		K_AK_sigma2	0,61	0,61	0,61	0,61
		K_AK_sigma3	0,61	0,61	0,61	0,61
	corrected principal stress	sigma_1_AK =	75,62	88,90	69,45	71,86
		sigma_2_AK =	89,13	88,90	84,88	87,83
		sigma_3_AK =	89,13	88,90	84,88	87,83
Safety factors		J_D	1,96	1,96	1,96	1,96
		delta_j (brittle	0,26	0,26	0,26	0,26
		J_ges	2,13	2,13	2,27	2,11
Fatigue assessment		a_BK_sigma1	**0,02**	**0,06**	**0,08**	**0,15**
		a_BK_sigma2	**0,22**	**0,28**	**0,21**	**0,28**
		a_BK_sigma3	**0,27**	**0,28**	**0,23**	**0,30**